

The FENIKS Survey: Stellar-Halo Mass Relationship of Central and Satellite Galaxies in UDS and COSMOS at $0.2 < z < 4.5$

KUMAIL ZAIDI ¹, DAVID A. WAKE ², DANILO MARCHESINI ¹, KARTHEIK IYER ^{3,4}, ADAM MUZZIN ⁵,
CASEY PAPOVICH ^{6,7}, JACQUELINE ANTWI-DANSO ³, KARL GLAZEBROOK ^{8,9} AND IVO LABBÉ ⁹

¹Tufts University, 574 Boston Avenue, Medford, MA 02155, USA

²Department of Physics and Astronomy, University of North Carolina Asheville, Asheville, NC 28804, USA

³David A. Dunlap Department of Astronomy & Astrophysics, University of Toronto, 50 St George St, Toronto, ON M5S 3H4, Canada

⁴Columbia Astrophysics Laboratory, Columbia University, 550 West 120th Street, New York, NY 10027, USA

⁵Department of Physics & Astronomy, York University, 4700 Keele Street Toronto, Ontario, M3J 1P3, Canada

⁶George P. and Cynthia Woods Mitchell Institute for Fundamental Physics and Astronomy, Texas A&M University, College Station, TX 77743, USA

⁷Department of Physics & Astronomy, Texas A&M University, 4242 TAMU, College Station, TX 77743, USA

⁸ARC Centre of Excellence for All Sky Astrophysics in 3 Dimensions (ASTRO 3D), Australia

⁹Centre for Astrophysics and Supercomputing, Swinburne University of Technology, Melbourne, VIC 3122, Australia

Submitted to ApJ

ABSTRACT

We present a comprehensive analysis of the observed Stellar-to-Halo mass relationship (SHMR) spanning redshifts from 0.2 to 4.5. This was enabled through galaxy clustering and abundance measurements from two large (effective area ~ 1.61 deg²) and homogeneously prepared photometric catalogs - UltraVISTA ultra-deep stripes DR3 (COSMOS) and FENIKS v1 (UDS). To translate these measurements into the SHMR, we introduce a novel halo occupation distribution (HOD) fitting approach (“smooth- z ”) whereby HOD parameters between neighboring z -bins are connected via physically motivated continuity (smoothing) priors. As a result, the high constraining power at $z \lesssim 2$, due to a much wider dynamical range in stellar mass (~ 3 dex), helps constrain the SHMR at $z \gtrsim 2$, where that range shrinks down to $\lesssim 1$ dex. We find that the halo mass is tightly coupled to star formation: the halo mass with peak integrated star-forming efficiency (SFE), M_h^{peak} remains constant within $\sim 10^{12.2} - 10^{12.4} M_\odot$ throughout the redshifts probed. Furthermore, we show that if we had relied on COSMOS alone (as opposed to COSMOS+UDS), as has been done by many preceding studies, M_h^{peak} would be systematically lower by up to ~ 0.15 dex at $z < 1.5$, highlighting the importance of mitigating cosmic variance. Finally, for the first time, we show how the SFE evolves with redshift as halos grow in mass along their progenitor merger trees, instead of at fixed halo masses.

1. INTRODUCTION

In the standard cold-dark matter with dark energy (Λ CDM) model, structure in the Universe forms hierarchically. Small seeds of primordial over-densities in the structure of the Universe, as evidenced through the cosmic microwave background radiation (CMB), grow larger over time. Since dark matter accounts for $\sim 84\%$ of the matter in the Universe (Planck Collaboration et al. 2020), through gravity, it guides the bulk of this evolution. Regions over-dense in dark matter grow in size, accumulate enough mass to become self-gravitating

halos, and decouple from the expansion of the Universe caused by dark energy. Within the potential wells of these halos, cold streams of gas funnel in, forming cold and dense clumps eventually reaching pressure, temperature, and density thresholds to trigger nuclear fusion - star formation and galaxy formation (White & Rees 1978; Fall & Efstathiou 1980; Springel et al. 2006).

Over time, halos grow in size and mass through merging and so do their resident galaxies. The evolution of dark matter halos and galaxies are intricately linked in this manner. To understand the influence of the aforementioned structure formation on galaxy formation and vice versa, we need to understand how galaxy properties like stellar mass are dictated by their host dark matter halo properties like mass, the so-called galaxy-halo connection (see Wechsler & Tinker (2018) for a review) and

vice versa. Our first hint into the galaxy-halo connection comes by comparing the abundance of halos – Halo mass functions (HMFs) from N -body simulations to the observed abundance of galaxies – Galaxy Stellar mass Functions (SMFs) (e.g. see [Legrand et al. \(2019\)](#) for a relatively recent example). Through this approach, it was realized early that galaxy formation is indeed a very inefficient process (e.g. [Conroy & Wechsler \(2009\)](#)). The SMFs have a much flatter slope at low mass than the HMFs, indicating inefficient star formation, and on the other hand, a much sharper decline at higher masses than the HMFs again indicating inefficient star formation.

Another facet of this inefficient star formation is the observationally constrained Stellar-Halo mass relationship (SHMR) itself ([Mandelbaum et al. 2006](#); [Moster et al. 2010](#)). The resulting stellar-to-halo mass ratio (M_*/M_h) at a given epoch is a strong indicator of how efficient the halos with the current mass, M_h have been throughout their history in converting available baryons into stars (“in-situ” star formation), and in the accretion of stellar matter through mergers (“ex-situ” star formation). M_*/M_h can be easily converted into this SFE by dividing it with the available baryonic fraction of the Universe, $f_b = \Omega_b/\Omega_m = 0.158$ ([Planck Collaboration et al. 2020](#)), where Ω_b and Ω_m are the baryonic and total matter (baryons+dark matter) density fractions.

Numerous low and high redshift observational data based studies - [Leauthaud et al. \(2012\)](#) out to $z \sim 1$, [Coupon et al. \(2012\)](#) out to $z \sim 1.2$, [Wake et al. \(2011\)](#) at $1 < z < 2$, [McCracken et al. \(2015\)](#) out to $z \sim 2$, [Cowley et al. \(2018\)](#) at $1.5 \lesssim z \lesssim 3$, [Legrand et al. \(2019\)](#) out to $z \sim 5$, [Shuntov et al. \(2022\)](#) out to $z \sim 5$, [Behroozi et al. \(2013\)](#) out to $z \sim 8$, and [Behroozi et al. \(2019\)](#) out to $z \sim 10$, either directly show or support that SFE remains low at all redshifts - on the order of a few percent. It peaks at most at $\sim 20\%$ at $M_h \sim 10^{12} M_\odot$, a mass which evolves mildly with redshift. At lower and higher halo masses, SFE drops sharply due to various feedback processes that suppress star formation. At the low mass end, it is thought to be stellar winds that expel or heat the surrounding gas and hot bubbles created by supernovae explosions that limit star formation ([Hopkins et al. 2012](#)). At the high mass end, active galactic nuclei (AGN) feedback specifically in ‘radio mode’ (radiatively inefficient, low accretion rate) is thought to shut down star formation ([Silk & Rees 1998](#); [Croton et al. 2006](#); [Kondapally et al. 2023](#); [Scharré et al. 2024](#)). This suppression in star formation at lower and higher halo masses relative to $\sim 10^{12} M_\odot$ also becomes visible in the deviation of the slopes at low/high mass of observed SMFs from the cosmological simulation-derived HMFs, as mentioned above.

As the observationally constrained SHMR is a result of the amalgamation of physical processes at various mass scales, it provides strong priors for the cutting-edge semi-analytic models such as Dark SAGE ([Stevens](#)

[et al. 2016, 2023](#)) and L-GALAXIES ([Henriques et al. 2015, 2020](#)), as well as suites of state-of-the-art hydrodynamical simulations such as IllustrisTNG ([Weinberger et al. 2017](#); [Pillepich et al. 2018](#)) and the FIRE project ([Wetzel et al. 2023](#); [Hopkins et al. 2023](#)). This unison of observations and simulations has been incredibly helpful in advancing our understanding of the galaxy-halo connection ([Somerville & Primack 1999](#); [Cole et al. 2000](#); [Springel et al. 2005](#); [Bower et al. 2006](#); [Croton et al. 2006](#); [De Lucia & Blaizot 2007](#); [Guo et al. 2011](#); [Vogelsberger et al. 2014](#); [Schaye et al. 2015](#); [Pillepich et al. 2018](#)). While the hydrodynamical simulations and semi-analytical models are incredibly helpful in informing the baseline understanding of the galaxy-halo connection, their conclusions are heavily dependent on assumptions related to gas dynamics, treatment of supernovae, and the implementation of the chosen *sub-grid* recipes beyond the resolution scale of the simulation, among others.

A more observation-dependent approach to constraining the relationship between assembly histories of dark matter halos and their resident galaxies is the so-called empirical modeling where physical priors come directly from observations. Several observational probes of galaxy formation such as star-formation rates, SMFs, quenched fractions, galaxy clustering, etc. are utilized in a self-consistent way to inform the creation of mock universes by populating halo merger trees (with galaxies) from dark matter-only simulations ([Behroozi et al. 2013](#); [Moster et al. 2018](#); [Behroozi et al. 2019](#)). Even though empirical models do not assume any models of galaxy formation, they adopt parametrizations to capture, e.g. star formation in halos based on halo properties and then further parameterize their redshift evolution, they too remain quite model-dependent. Moreover, the inter-observational systematics, resulting from combining large amounts of data from several surveys with differently calibrated data reduction pipelines, are bound to skew the results.

Perhaps the simplest approach to connecting galaxies to their host halos is to match their abundances – ‘abundance matching’ ([Marinoni & Hudson 2002](#); [Conroy & Wechsler 2009](#); [Behroozi et al. 2010](#)). In this method, the halos are usually rank-ordered by their mass and assigned the rank-ordered galaxies by stellar mass (or luminosity) individually. The idea is simple; the more massive a galaxy, the more massive its host. However, just matching abundances ignores the galaxy-halo connection information hidden in the structure on all scales which can be measured via clustering. Clustering on small scales contains information on how the satellite galaxies are distributed within a halo and on large scales how both the central and satellites are distributed. Furthermore, since clustering is directly related to halo mass, it is an indirect probe on the halo mass, which combined with the information contained in SMFs, provides tighter constraints on the galaxy-halo connection

(Behroozi et al. 2010; Coupon et al. 2015). Finally, if we keep the abundances of stellar mass and halo mass unchanged but tweak the scatter in stellar mass at fixed halo mass, we will assign the galaxies to halos differently resulting in a change in clustering (Wechsler & Tinker 2018). Therefore, measurements of clustering, beyond helping constrain the halo mass, allow constraining the scatter in stellar mass (at fixed halo mass) better.

The observations of both galaxy clustering and abundance can be leveraged to break degeneracies as mentioned above to get a robust estimate of SHMR within the framework of Halo occupation distribution (HOD) modeling. The HOD model simply populates halos of different masses with different numbers of galaxies, on average, and is split between contributions from central and satellite galaxies in the traditional HOD models (Zheng et al. 2005, 2007; Zehavi et al. 2005, 2011; Leauthaud et al. 2011; Zu & Mandelbaum 2015). Besides having centrals and satellites, galaxies can be further split into contributions from star-forming and passive galaxies as in the Tinker et al. (2013) and Zu & Mandelbaum (2016) HOD models.

A chosen HOD model in combination with an adopted HMF from simulations and a few more ingredients (halo density profile, halo mass-concentration relation, etc.) can be used to model a power spectrum that would be produced by a distribution of galaxies on the sky, or in other words – galaxy clustering. The HOD parameters that produce this clustering and the abundance can then be fine-tuned by fitting against the observations of galaxy clustering and the highly constraining galaxy abundance (SMFs). A constrained HOD model then gives the SHMR and many other interesting quantities such as the fraction of galaxies that are satellites as opposed to centrals in a halo of a given mass. HOD model fitted at different redshifts allows us to trace the assembly of central and satellite galaxies and since it does not assume any galaxy formation physics but is purely observation-dependent in that regard, it gives us clues into unknown astrophysical phenomena that might be at play. This is especially true at high redshift where our understanding of overall galaxy formation remains quite extrapolated.

Besides being constrained by the observations of galaxy clustering and abundance, the HOD model can additionally incorporate constraints from galaxy-galaxy lensing observations. For instance, Leauthaud et al. (2012) combined all of the three probes: galaxy clustering, galaxy abundance, and galaxy-galaxy lensing to constrain the HOD, and thus SHMR out to $z \sim 1$ using data in the COSMOS field (Scoville et al. 2007a), although, lensing observations prove difficult at $z > 1$.

To set the stage for our paper, below we highlight a few recent contributions in the literature that constrain the SHMR and the corresponding M_h^{peak} through observations of clustering and abundance under the framework of HOD:

Ishikawa et al. (2017) measured the SHMR by fitting the Zheng et al. (2005) HOD with clustering and abundance of u -, g -, and r - dropout galaxies at $z \sim 3, 4$ and 5 , respectively. They find that M_h^{peak} climbs up steadily from $10^{11.92 \pm 0.097} M_\odot$ at $z \sim 5$ to $10^{12.25 \pm 0.053} M_\odot$ at $z \sim 3$, opposite of the expectation from *downsizing* (Cowie et al. 1996) in which case the M_h^{peak} should decline with time. However, this was in agreement with the empirical modeling (Behroozi et al. 2013).

Using the Zheng et al. (2007) HOD, Cowley et al. (2018) probed the SHMR at $1.5 \lesssim z \lesssim 5$ leveraging the *Spitzer* IRAC 3.6 and $4.5 \mu\text{m}$ data (SMUVS survey (Ashby et al. 2018) within the UltraVISTA ultra-deep stripes (McCracken et al. 2012) of the COSMOS field (Scoville et al. 2007a). They were the first to use a stellar mass-selected sample to constrain the M_h^{peak} at $z \sim 2.5$ which was found to be $10^{12.5^{+0.10}_{-0.08}} M_\odot$, a mild increase from lower redshifts, consistent with *downsizing*.

Most recently, using the Leauthaud et al. (2011, hereafter L11) HOD, Shuntov et al. (2022) constrained the SHMR out to $z \sim 5$ by utilizing a large homogeneously prepared catalog – COSMOS2020 (Weaver et al. 2022) covering an effective area of 1.27 deg^2 in a single field. For the first time with a stellar mass-selected sample, they extended the redshift frontier for M_h^{peak} out to $z \sim 5$, showing a drop of ~ 1 dex going from $10^{12.94^{+0.36}_{-0.34}} M_\odot$ at $z \sim 5$ to $10^{12.07^{+0.07}_{-0.07}} M_\odot$ at $z \sim 0.35$, a strong *downsizing* (Cowie et al. 1996) signal indeed. However, their uncertainty on M_h^{peak} at $z \sim 5$ spans a large range of ~ 0.8 dex. This is primarily because the sample remains complete only for the massive galaxies ($M_* \gtrsim 10^{10} M_\odot$) at high- z , thus providing no constraints on the low-mass end of the SHMR.

In this paper, we constrain the relationship between galaxy stellar mass and their host dark matter halo mass using HOD modeling. Out to $z \sim 5$, this study is the first to use a large total effective area of $\sim 1.61 \text{ deg}^2$ evenly split between two fields: UDS $\sim 0.79 \text{ deg}^2$ and COSMOS $\sim 0.82 \text{ deg}^2$ which greatly reduces the effect of cosmic variance in measurements. The availability of deep optical to mid-IR photometry in both fields leads to robust redshifts and stellar population properties allowing accurate measurement of galaxy clustering and abundance. More importantly, the photometric catalogs in both fields are homogeneously prepared so they are free from systematic biases affecting the interpreted SHMR (Behroozi et al. 2013; Moster et al. 2018; Behroozi et al. 2019). Much of the previous work in observationally deriving SHMR is based on the single COSMOS field (e.g. Cowley et al. 2018; Legrand et al. 2019; Shuntov et al. 2022). We show that by adding the UDS field, the resulting SHMR changes drastically, indicating that the scatter in SHMR might be dependent on the environment.

Another novel aspect of this work is to jointly fit the galaxy clustering and abundance data in the entire redshift range of $0.2 < z < 4.5$ by imposing smooth continuity priors on the redshift evolution of the HOD parameters. Tying together the z -bins in this way allows us to constrain the evolution of SHMR with higher confidence, especially at high redshift $z \gtrsim 2$ where the sample is complete only for the most massive galaxies ($M_* \gtrsim 10^{10} M_\odot$). This would not have been possible if, following the usual procedure in the literature (e.g. Shuntov et al. (2022)), we had solely relied on the weaker constraining power of the individual z -bins at high redshift. Finally, we trace the SFE of halos as they grow in mass along their merger trees in the TNG300-1-Dark simulation (Pillepich et al. 2018).

The paper is structured as follows: In Section 2, we present the photometric catalogs utilized in this study and the sample selection. Section 3 describes the methodology used to measure galaxy clustering and abundance (SMF) ultimately used to constrain the HOD models. The adopted HOD modeling along with our new approach of fitting individual z -bins connected through smooth continuity priors is detailed in Section 4. This is followed by our SHMR results presented in Section 5. In section 6, we discuss the intuition gained based on the results about the assembly of centrals and satellites and their host halos. We conclude with a summary in Section 7.

Throughout this paper, we adopt a flat Λ CDM cosmology with the following parameter values at $z = 0$ (denoted by the subscript ‘0’): Hubble constant, $H_0 = 70 \text{ km s}^{-1} \text{ Mpc}^{-1}$; matter density, $\Omega_{m,0} = 0.3$ with a baryon fraction of 15.8% (Planck Collaboration et al. 2020) giving baryon density, $\Omega_{b,0} = 0.0474$; dark energy density, $\Omega_{\Lambda,0} = 0.7$; cosmic microwave background (CMB) temperature, $T_{cmb,0} = 2.7255 \text{ K}$. The masses are always quoted with the implicit dependence on the dimensionless scaled Hubble constant, $h = 0.7$ (complying with the H_0 given above): $M_\odot h^{-1}$ for dark matter halo masses and $M_\odot h^{-2}$ for the stellar masses. Furthermore, in the derivation of stellar population properties, we assumed the Chabrier initial mass function (IMF; Chabrier (2003)) and the Calzetti dust attenuation law (Calzetti et al. 2000).

2. DATA

2.1. COSMOS and UDS catalogs

For this study, we utilize two homogeneously prepared catalogs in the COSMOS (UVISTA (Muzzin et al. 2013) DR3, ultra-deep stripes) and UDS (Zaidi et al. 2024) fields. These catalogs are based on deep, multi-wavelength Optical-NIR (IRAC) photometry in 50 and 24 filters for COSMOS and UDS, respectively.

The photometric redshifts are derived using the SED template fitting code EAZY (Brammer et al. 2008) for COSMOS and its python implementation eazy-py for UDS. The photo- z ’s agree with the available spectro-

scopic redshifts well. Within the redshift span probed in this study $-0.2 < z < 4.5$, for COSMOS, the normalized median absolute deviation, $\sigma_{\text{NMAD}} = 0.00505$, and the catastrophic outlier percentage ($\frac{\Delta z}{1+z_{\text{spec}}} > 0.15$) is $\sim 1.60\%$. For the same redshift span, for UDS, $\sigma_{\text{NMAD}} = 0.01242$, while the catastrophic outlier percentage is $\sim 2.38\%$. The details on the spectroscopic redshifts considered for these analyses are mentioned in Zaidi et al. (2024) for UDS and Muzzin et al. (2013) for COSMOS. As spectroscopic redshifts are dominated by bright objects, we also addressed this bias in Zaidi et al. (2024) for UDS by estimating the photo- z errors for the full catalog using the redshift-pair method (Quadri & Williams 2010). We found the photo- z errors to be within $\sim 0.7\text{--}4.5\%$ depending on redshift, stellar mass and K -band magnitude considered.

The stellar masses along with other stellar population parameters were derived using the Dense Basis code (Iyer & Gawiser 2017; Iyer et al. 2019) which uses non-parametric star formation histories (SFHs) that are able to robustly capture different types of stellar populations giving unbiased estimates of stellar population properties as opposed to the codes implementing a singular functional form for SFH (Mowla et al. 2022). As shown in Zaidi et al. (2024), the FAST code (Kriek et al. 2009) implementing a singular functional form for star-formation history, a delayed-exponential, provides systematically lower stellar masses by ~ 0.4 dex at $M_* \lesssim 10^{10} M_\odot$. Therefore, we also report the effect of this stellar mass offset in §5.4. In both cases, we assumed the Chabrier (2003) IMF and the Calzetti et al. (2000) dust attenuation law.

2.2. Sample selection

To measure the clustering and the SMF reliably, we select galaxies with robust photometry meaning that they are i- identified as a galaxy (not a star), ii- do not fall on contaminated pixels which can be due to the proximity to nearby bright stars or other image artifacts, and are brighter than the 90% completeness limit in the detection band (see below for details). This selection was achieved using the masks generated for bright stars/artifacts/bad pixels and the following catalog cuts. For COSMOS, `use = 1`, `star = 0`, `contamination = 0`, `nan_contam < 3`, `K_flag ≤ 3` , `15 < total mag $_{K_s}$ [AB] < 24.5` (90% completeness), and similarly for UDS, `use_phot = 1`, `flag_Kuds ≤ 3` , `total mag $_K$ [AB] < 24.3` (90% completeness). Additionally for UDS, we also avoid noisy data found along the four sides of the image. After such exclusions, we are left with the effective areas of 2954.51 arcmin^2 ($\sim 0.82 \text{ deg}^2$) in COSMOS and 2828.25 arcmin^2 ($\sim 0.79 \text{ deg}^2$) in UDS which equals a combined effective area of $\sim 1.61 \text{ deg}^2$.

We determined the completeness for both COSMOS and UDS by calculating the recovered detections of injected stars in the images as a function of magnitudes in the detection bands, K_s and K for COSMOS and UDS,

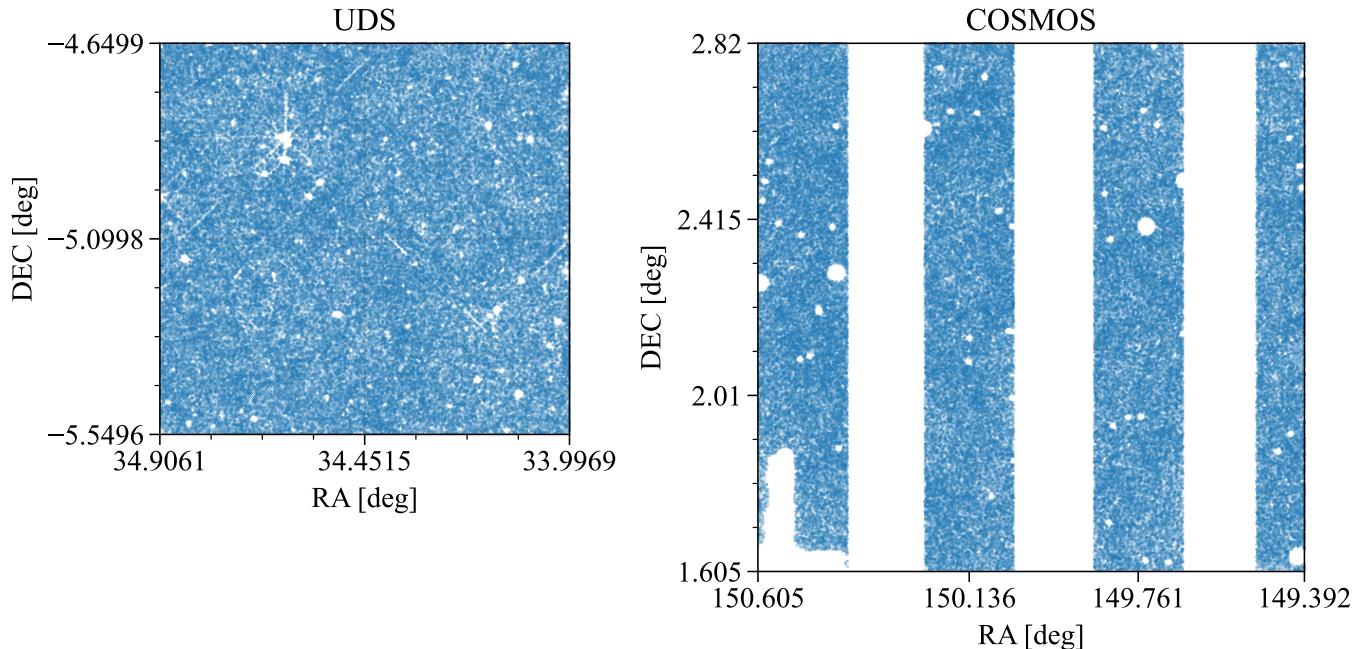


Figure 1. The final sample of galaxies selected in UDS ($N = 143,549$) and COSMOS ($N = 166,826$) is shown in blue points. The irregularly shaped white patches within both fields represent masked areas due to bright stars and other artifacts. In COSMOS, only ultra-deep stripes of the UltraVISTA DR3 survey are utilized, while the shallower deep stripes, visible in white, are excluded. The relative dimensions of the panels highlight the relative RA/DEC span of the two fields. The effective areas of UDS and COSMOS are $\sim 0.79 \text{ deg}^2$ and $\sim 0.82 \text{ deg}^2$, respectively. This amounts to a total effective area of $\sim 1.61 \text{ deg}^2$.

respectively. We injected the stars at random locations on the images allowing for overlap with other sources to mimic the original images where some overlap is natural. The 90% completeness in the detection K_s -band for COSMOS is 24.5 AB whereas the 90% completeness in the detection K -band for UDS is 24.3 AB.

Then, we used these estimates of 90% K_s/K completeness limits to derive the stellar mass completeness for both fields separately following the method outlined in [Juneau et al. \(2005\)](#) and [Pozzetti et al. \(2010\)](#). We scaled the stellar masses of galaxies as a function of redshift to the masses they would have if they were at the limiting magnitudes mentioned above. This gives a representative distribution of mass-to-light (M/L) ratios for our two fields at the limiting magnitudes. We chose the 80th percentile of this distribution as a function of redshift as the stellar-mass limit (80% stellar mass completeness) above which most galaxies are observable.

Finally, we restrict our combined sample (UDS+COSMOS) in this study to the higher of the two 80% stellar mass completeness limits in UDS and COSMOS which lie very close to each other as shown in [Fig. 2](#). Our final sample, divided into 9 z -bins within $0.2 < z < 4.5$ and further into stellar mass threshold (M_*^t) samples, is marked with black lines (“ladders”) in [Figure 2](#) and listed in [Table 1](#). Note that the sub-samples are cumulative as opposed to binned in stellar mass, i.e. each stellar mass threshold sample contains all the

galaxies within the stellar mass threshold samples below it.

Besides, the complete stellar mass indeed evolves within each z -bin, as visible by the non-horizontal completeness curve. Therefore, to fix our lowest stellar mass threshold within each z -bin, we chose it to be at the intersection of the completeness curve with the highest redshift end of any z -bin. These are the bottom right corners of the black “ladders” within each z -bin in [Figure 2](#). By doing so, we ensure that any z -bin sample is at least 80% complete throughout the redshift thickness of its bin. Within each z -bin, the samples become more and more complete as the redshift decreases.

Now, we address the consequence of our choice of the lower limit in stellar mass completeness – 80% instead of 95% or 100%. By choosing 80%, we miss some galaxies with the highest M_*/L_* ratios lying close to the bottom-right corners of the lowest mass threshold samples within each z -bin. However, such high M_*/L_* ratio galaxies, which are old and dusty (passive), are extremely rare at such stellar masses. The breakdown of SMFs into star-forming and passive galaxies at $0.5 \lesssim z \lesssim 2.5$ ([Santini et al. 2022](#)) shows that passive galaxies are ~ 40 – 60% rarer at the stellar masses near our completeness curve.

This means that within the lowest mass threshold samples, we miss an incredibly small fraction of galaxies that lie close to the bottom-right corners of the “ladders”. Therefore, the lowest mass threshold samples we use in this study are very close to the true completeness

Table 1. Sub-samples used in this study

z -bin	$\log_{10}(M_*^t [M_\odot])$	N_{COSMOS}	N_{UDS}	N_{total}
$0.2 < z < 0.5$	8.6	12386	9681	22067
	9.0	8359	6068	14427
	9.5	4988	3460	8448
	10.0	2963	2056	5019
	10.5	1524	1032	2556
$0.5 < z < 1.0$	9.3	25173	21628	46801
	9.6	19056	14648	33704
	10.1	11357	7481	18838
	10.6	5861	3625	9486
	11.0	2333	1212	3545
$1.0 < z < 1.25$	9.4	9119	9385	18504
	9.8	6234	5640	11874
	10.2	3905	2967	6872
	10.6	2306	1504	3810
	10.8	1644	951	2595
$1.25 < z < 1.5$	9.6	7598	11131	18729
	9.9	5493	7304	12797
	10.2	3746	4381	8127
	10.5	2388	2423	4811
	10.7	1663	1547	3210
$1.5 < z < 1.75$	9.6	4720	6341	11061
	10.1	2556	3448	6004
	10.5	1278	1622	2900
	10.7	843	999	1842
$1.75 < z < 2.25$	9.8	7067	7647	14714
	10.1	4942	4714	9656
	10.3	3606	3143	6749
	10.5	2506	1890	4396
$2.25 < z < 2.75$	9.9	4689	4664	9353
	10.2	2695	2685	5380
	10.5	1211	1227	2438
$2.75 < z < 3.5$	10.1	2984	4839	7823
	10.2	2348	3587	5935
	10.4	1217	1650	2867
$3.5 < z < 4.5$	10.3	589	1603	2192
	10.35	514	1280	1794

in stellar mass, and any higher mass threshold samples are essentially complete.

3. MEASUREMENTS

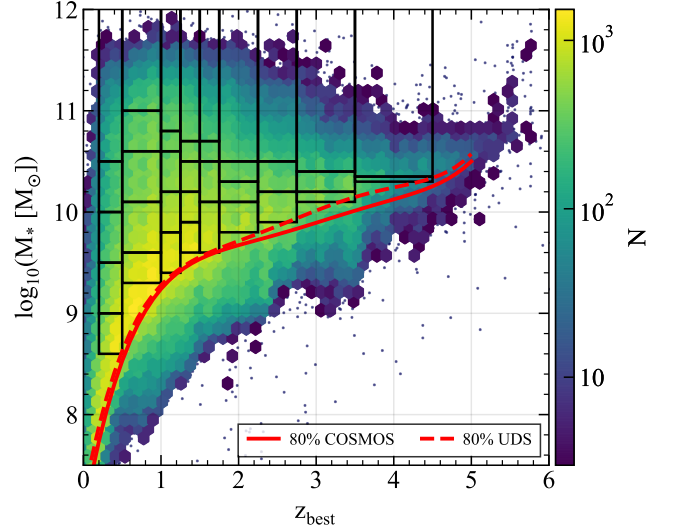


Figure 2. Distribution of the stellar mass versus redshift of the galaxies in COSMOS and UDS along with the selected sub-samples (black ladders) for this study. The rungs of the ladders show the mass thresholds (for clustering) and mass bins (for SMF) of the sub-samples. The right edge of the bottom rung of the ladders at each redshift corresponds to the higher of the solid red and dashed red curves, representing the 80% stellar mass completeness of COSMOS and UDS, respectively.

3.1. Two-point angular correlation function

We compute the two-point angular correlation function, $w_{obs}(\theta)$ for the stellar mass threshold samples which is essentially the excess probability above Poisson of finding a galaxy-galaxy pair as a function of angular scale, θ . To do so, we use the popular [Landy & Szalay \(1993\)](#) estimator shown in Eq.1 within the python-based pair counter engine, `CORRFUNC`¹ ([Sinha & Garrison 2020](#)) implemented within the python utility wrapper, `pycorr`². In Eq.1, DD , DR , and RR , indicate the number of data-data, data-random, and random-random pairs. All of these pairs are normalized by the total number of possible pairs, as shown in Eq.1 where, n_D and n_R indicate the number of points in the data and random catalogs, respectively.

$$w_{obs}(\theta) = \frac{\left[\frac{DD(\theta)}{n_D^2} - 2 \frac{DR(\theta)}{n_D n_R} + \frac{RR(\theta)}{n_R^2} \right]}{\left[\frac{RR(\theta)}{n_R^2} \right]}. \quad (1)$$

The random catalog is created using exactly the same survey geometry mapped out by the galaxies considered in this study avoiding areas around bright stars, etc. Moreover, the number of points in the random catalogs

¹ <https://github.com/manodeep/Corrfunc>

² <https://github.com/cosmodesi/pycorr>

are at least ~ 65 times more than the galaxies in any stellar mass threshold sample ensuring that $w_{obs}(\theta)$ is properly measured. We measure the $w_{obs}(\theta)$ in 13 angular separation bins within $-3 < \log_{10}(\theta[\text{deg}]) < -0.6$ which corresponds to a maximum separation of just over 0.25 deg. As a result we probe a maximum transverse co-moving scale of ~ 6 Mpc in our lowest z -bin which increases to ~ 32 Mpc for our highest z -bin.

We estimate the errors on $w_{obs}(\theta)$ by calculating the square root of the diagonal elements of the covariance matrix capturing the covariance among all angular scales. To estimate the covariance matrix, we use the ‘delete-one’ jackknife method (Wall & Jenkins 2012) wherein we subdivide the whole region of our sample footprint into 50 equal-sized patches. Then for each mass threshold sample, we compute the correlation functions for 50 realizations each time with a unique patch removed. Finally, for each sub-sample, the covariance matrix, C_{ij} is computed as follows:

$$C_{ij} = \frac{N_r}{N_r - 1} \sum_{r=1}^{N_r} (w_r(\theta_i) - \tilde{w})^T (w_r(\theta_j) - \tilde{w}), \quad (2)$$

where N_r is the number of realizations, \tilde{w} is the average correlation function of all realizations and i and j indices label the angular separation bins.

As we measure $w_{obs}(\theta)$ from limited-sized patches on the sky (total effective area $\sim 1.61 \text{ deg}^2$), it is bound to be underestimated by a constant integral constraint (IC) factor (Groth & Peebles 1977). The IC correction scales inversely with the field size and directly with the clustering strength as it is equal to the fractional variance on galaxy counts (Wake et al. 2011). We describe how we deal with this correction in §4.6.

3.2. Redshift Distributions

In order to convert the modeled two-point correlation function in three dimensions $\xi(r)$ into angular correlation functions, $w_{model}(\theta)$ (as discussed in §4.6), we need the redshift distributions, $N(z)$, for each of the z -bins in our sample. We derived them by stacking the redshift probability distributions, $p(z)$ ’s of galaxies given by **eazy-py** within each z -bin ensuring that the 16th/84th percentiles lie within the limits of z -bins. The final $N(z)$ ’s are shown in Figure 3 where the large-scale structure can be easily gleaned through their jagged nature - sharp spikes and dips.

3.3. Stellar Mass Function

We derive the SMFs in the UDS and COSMOS fields above the lowest stellar masses threshold at each z -bin as described in §2.2, defined in Table 1 and shown in Figure 2. As we only compute SMFs for essentially complete samples, we do not need to implement the usual $1/V_{max}$ technique (Schmidt 1968) or similar, useful when not all of the galaxies within a stellar mass bin are observable

within the full volume spanned by a given z -bin and survey area.

The Poisson errors on the SMFs were estimated using Gehrels (1986) specially useful for small number counts at the high mass end. We also calculated cosmic variance errors for each of the two fields separately following Moster et al. (2011) and then combined them using the volume-weighted average technique described in the same paper. Finally, the total uncertainties on the SMFs were calculated by adding the Poisson errors and the errors due to cosmic variance in quadrature. We tabulate the combined SMFs in Appendix A.

4. MODELING THE HOD

We derive the SHMR under the framework of HOD which models the average number of galaxies selected above a stellar mass threshold as a function of halo mass. There are many implementations of it in the literature (e.g. Zheng et al. 2005, 2007; Zehavi et al. 2005, 2011; Leauthaud et al. 2011; Zu & Mandelbaum 2015) most of which at least split the contribution from the central galaxy and satellite galaxies to the average total occupation number at a given halo mass. The central galaxy is the most massive galaxy dominating the potential well of a halo and depending on the halo mass, it might be surrounded by one or more lower-mass satellite galaxies.

The clustering measurements are an amalgamation of galaxy-galaxy (central-satellite) pairs within the *same* halos and therefore dominant at smaller angular scales, and the galaxy-galaxy (central-central or central-satellite) pairs of different halos that contribute more at larger scales. These are the so-called ‘1-halo’ (pairs from the *same* halos) and ‘2-halo’ (pairs from *different* halos) contributions to the total clustering which result in a break in total clustering at a certain angular scale where the clustering strength of ‘1-halo’ drops and ‘2-halo’ picks up (Zehavi et al. 2004).

4.1. SHMR of Central Galaxies

In this study, we utilize the HOD prescribed by L11 which starts by assuming a functional form for SHMR, $f_{\text{SHMR}}(M_h)$ which gives the mean-log stellar mass, $\langle \log_{10}(M_*(M_h)) \rangle$ for central galaxies as a function of a fixed halo mass, M_h . L11 adapted the $f_{\text{SHMR}}(M_h)$ from Behroozi et al. (2010). For convenience, $f_{\text{SHMR}}(M_h)$ can be inversely defined as follows:

$$\log_{10}(f_{\text{SHMR}}^{-1}(M_*)) = \log_{10}(M_h) = \log_{10}(M_1) + \beta \log_{10} \left(\frac{M_*}{M_{*,0}} \right) + \frac{\left(\frac{M_*}{M_{*,0}} \right)^\delta}{1 + \left(\frac{M_*}{M_{*,0}} \right)^{-\gamma}} - \frac{1}{2}, \quad (3)$$

where M_1 governs the characteristic halo mass, the higher its value, the more massive the host halo for

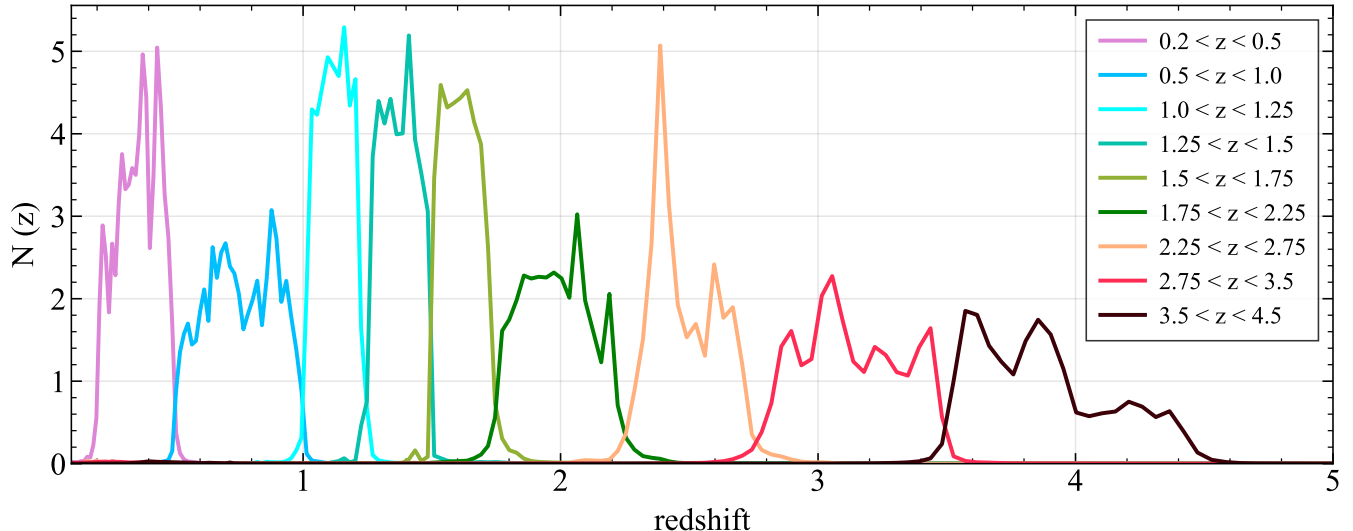


Figure 3. Redshift distribution, $N(z)$ for each of the 9 bins used in this study generated by stacking the galaxies’ redshift probability distributions given by `eazy-py`.

a given stellar mass; $M_{*,0}$, in turn, governs the characteristic stellar mass, such that increasing it results in less massive host halos assigned to a given stellar mass; β controls the power-law slope at the low-mass end; whereas δ controls the sub-exponential slope on the high-mass end; finally, γ dictates how sharp the transition is between the low-mass and high-mass regimes. The effect of varying each of these parameters on the shape of SHMR can also be seen through Figure 1 in L11.

4.2. Scatter in Stellar Mass at a fixed Halo mass

At a fixed halo mass there is still expected to be a scatter in the stellar mass, which arises from the intrinsic scatter in the Universe and the scatter introduced by measurement errors due to SED modeling, photo- z uncertainties, and the errors in the observed magnitudes (Behroozi et al. 2010; L11). L11 captures this stochasticity by assuming a log-normal distribution describing the probability distribution function of $\log_{10}(M_*)$ at a fixed halo mass. The standard deviation of this distribution, $\sigma_{\log M_*}$, the log-normal scatter in the stellar mass at a fixed halo mass is then fitted as a free parameter.

As our samples are always selected based on stellar mass (not halo mass), they are quite sensitive to scatter in halo mass, $\sigma_{\log M_h}$ (L11). Moreover, the SHMR turns from a power-law to sub-exponential beyond a certain stellar mass; the halo mass, and as a result, the $\sigma_{\log M_h}$ rises sharply. At the high-mass end, small increments in stellar mass lead to larger jumps in the $\sigma_{\log M_h}$. This means that the data at the high mass end is more constraining for the scatter ($\sigma_{\log M_h}$ or $\sigma_{\log M_*}$) than the data at the low mass end (Leauthaud et al. 2012). Therefore, the inclusion of halo mass dependence in $\sigma_{\log M_*}$ does not matter in any meaningful way as $\sigma_{\log M_*}$ is hard to measure at low M_* due to its weak imprint on the data.

In fact, Leauthaud et al. (2012) considered two models, one in which $\sigma_{\log M_*}$ is a constant and another in which it varies as a function of stellar mass. They found no meaningful differences in the resulting HOD parameter fit and the SHMR model. As a consequence, we have assumed $\sigma_{\log M_*}$ to be independent of halo mass in this work, i.e. $\sigma_{\log M_*}$ is considered to be constant for all halo masses within a z -bin.

4.3. Mean Occupation of Central Galaxies

To compute the mean occupation of central galaxies, we can integrate the conditional SMF for centrals, $\Phi_{cen}(M_*|M_h)$ which is the number of centrals with stellar mass within $M_* \pm dM_*/2$, given a fixed halo mass. For instance, for a sample of centrals with a stellar mass threshold, M_*^t , the mean occupation can be calculated as follows:

$$\langle N_{cen}(M_h|M_*^t) \rangle = \int_{M_*^t}^{\infty} \Phi_{cen}(M_*|M_h) dM_* \quad (4)$$

In L11, $\Phi_{cen}(M_*|M_h)$ is defined as log-normal distribution (see their Equation 1) which means that $\langle N_{cen}(M_h|M_*^t) \rangle$ can be derived analytically. The final expression for $\langle N_{cen}(M_h|M_*^t) \rangle$ using $f_{\text{SHMR}}(M_h)$ and a constant $\sigma_{\log M_*}$ then becomes (see L11 for the shape of $\langle N_{cen}(M_h|M_*^t) \rangle$ at different M_*^t):

$$\langle N_{cen}(M_h|M_*^t) \rangle = \frac{1}{2} \left[1 - \text{erf} \left(\frac{\log_{10}(M_*^t) - \log_{10}(f_{\text{SHMR}}(M_h))}{\sqrt{2}\sigma_{\log M_*}} \right) \right], \quad (5)$$

where the error function, erf is defined by

$$\text{erf}(x) = \frac{2}{\sqrt{\pi}} \int_0^x e^{-t^2} dt.$$

The alternate commonly employed expression for the mean occupation function of centrals in the literature, e.g. as in [Zheng et al. \(2005\)](#), can be derived from Equation 5 if: i- $f_{\text{SHMR}}(M_h)$ is assumed to be a power-law at all masses, and ii- a minimum halo mass, M_{min} , which corresponds to M_*^t , is introduced, i.e. $M_{\text{min}} \equiv f_{\text{SHMR}}^{-1}(M_*^t)$ ([L11](#)). Even though this common version agrees well with the Eq. 5 at low masses ($M_{\text{min}} \lesssim 10^{12} M_\odot$), the difference between the two grows between 10% – 40% at higher masses ([L11](#)) as the [L11](#) SHMR deviates from the power-law and becomes sub-exponential at high masses. As observations confirm that SHMR rises faster than a power-law at high masses, it is crucial to use an expression for $\langle N_{\text{cen}} \rangle$ that explicitly incorporates a shift from power-law to sub-exponential at higher masses.

4.4. Mean Occupation of Satellite Galaxies

The model for the mean occupation of satellites is expected to follow a power-law at high masses with an exponential sharp cut-off at low masses ([Berlind et al. 2003](#); [Kravtsov et al. 2004](#); [Zheng et al. 2005](#)). Therefore, the expression for $\langle N_{\text{sat}} \rangle$ can be written as in Eq. 6 where the α_{sat} is the power-law slope with M_{sat} as the power-law amplitude. M_{cut} defines the scale for the exponential cut-off. Moreover, halos are not expected to have satellite galaxies before having a central galaxy. This is ensured by scaling to the satellite occupation to $\langle N_{\text{cen}} \rangle$.

$$\langle N_{\text{sat}}(M_h|M_*^t) \rangle = \langle N_{\text{cen}}(M_h|M_*^t) \rangle \left(\frac{M_h}{M_{\text{sat}}} \right)^{\alpha_{\text{sat}}} \exp\left(\frac{-M_{\text{cut}}}{M_h} \right). \quad (6)$$

As it turns out according to the observational studies, M_{sat} is proportional to M_{min} , where M_{min} is the inverse of the SHMR, i.e. $M_{\text{min}} \equiv f_{\text{SHMR}}^{-1}(M_*^t)$, where $f_{\text{SHMR}}^{-1}(M_*^t)$ is assumed to be a power-law ([L11](#)). For added flexibility, instead of M_{sat} and M_{cut} simply scaling with $f_{\text{SHMR}}^{-1}(M_*^t)$, [L11](#) defines M_{sat} and M_{cut} as power-law functions of $f_{\text{SHMR}}^{-1}(M_*^t)$ as shown in Eq. 7 and Eq. 8, respectively.

$$\frac{M_{\text{sat}}}{10^{12} M_\odot} = B_{\text{sat}} \left(\frac{f_{\text{SHMR}}^{-1}(M_*^t)}{10^{12} M_\odot} \right)^{\beta_{\text{sat}}}, \quad (7)$$

$$\frac{M_{\text{cut}}}{10^{12} M_\odot} = B_{\text{cut}} \left(\frac{f_{\text{SHMR}}^{-1}(M_*^t)}{10^{12} M_\odot} \right)^{\beta_{\text{cut}}}. \quad (8)$$

Furthermore, we can easily calculate the fraction of stellar mass locked up in satellites, f_{sat} by dividing the mean number density of satellites, $\tilde{n}_{g, \text{sat}}$ with the mean total (central+satellites) number density, \tilde{n}_g , as shown in Equation 9 below. Here, the mean number densities are calculated by integrating the HMF, dn/dM_h along with the desired mean occupation function.

$$f_{\text{sat}} = \frac{\tilde{n}_{g, \text{sat}}}{\tilde{n}_g} = \frac{\int dM_h \frac{dn}{dM_h} \langle N_{\text{sat}}(M_h|M_*^t) \rangle}{\int dM_h \frac{dn}{dM_h} \langle N_{\text{total}}(M_h|M_*^t) \rangle} \quad (9)$$

4.5. Total Stellar Mass in Halos

The [L11](#) HOD model also allows us to conveniently calculate the total stellar mass in galaxies as a function of halo mass and the contributions from central and satellite galaxies. The total stellar mass within a stellar mass bin can be calculated by integrating the conditional SMFs of centrals and satellites multiplied by M_* with the stellar mass range as the limits of integration as shown in the second line of Equation 10. Then, using the fact that integrating the conditional SMF of centrals/satellites gives the occupation number of centrals/satellites and the integration by parts rule, we can further simplify the integration as shown in the third and fourth lines of Equation 10:

$$\begin{aligned} M_*^{\text{tot}}(M_h|M_*^{t_1}, M_*^{t_2}) = & \int_{M_*^{t_1}}^{M_*^{t_2}} [\Phi_c(M_*|M_h) + \Phi_s(M_*|M_h)] M_* dM_* = \\ & \int_{M_*^{t_1}}^{M_*^{t_2}} \langle N_{\text{cen}}(M_h|M_*) \rangle dM_* - [\langle N_{\text{cen}}(M_h|M_*) \rangle M_*]_{M_*^{t_1}}^{M_*^{t_2}} \\ & + \int_{M_*^{t_1}}^{M_*^{t_2}} \langle N_{\text{sat}}(M_h|M_*) \rangle dM_* - [\langle N_{\text{sat}}(M_h|M_*) \rangle M_*]_{M_*^{t_1}}^{M_*^{t_2}}, \end{aligned} \quad (10)$$

where the first term (third line) reflects the contribution from the central galaxies and the second term (fourth line) corresponds to the satellite galaxies.

4.6. Two-point angular correlation function from the HOD

To derive the modeled two-point angular correlation function, $w_{\text{halomod}}(\theta)$ within the `halomod` code ([Murray et al. 2021](#)), we start from the model galaxy real-space correlation function, $\xi_{gg}(r)$, the derivation of which is described in detail in [Murray et al. \(2021\)](#). Briefly, $\xi_{gg}(r)$ is connected to the galaxy power spectrum, $P_{gg}(k)$ via order-1/2 *Hankel* transform:

$$\xi_{gg}(r) = \frac{1}{2\pi^2} \int_0^\infty P_{gg}(k) k^2 j_0(kr) dk, \quad (11)$$

with j_0 being the zeroth-order spherical Bessel function, $j_0(x) = \frac{\sin x}{x}$. $P_{gg}(k)$ is further divided into contributions from the 1-halo (1h) and 2-halo (2h) pairs: $P_{gg}(k) = P_{gg}^{1h}(k) + P_{gg}^{2h}(k)$, and correspondingly, $\xi_{gg}(r) = [1 + \xi_{gg}^{1h}(r)] + \xi_{gg}^{2h}(r)$. $P_{gg}^{1h}(k)$ and $P_{gg}^{2h}(k)$ are defined as follows:

$$P_{gg}^{1h}(k) = \int dM_h \frac{dn}{dM_h} u(k|M_h) \left[\langle N_{sat} \rangle^2 u(k|M_h) + 2 \langle N_{sat} N_{cen} \rangle \right], \quad (12)$$

$$P_m^{2h}(k) = P_m(k) \left[\int dM_h \frac{dn}{dM_h} u(k|M_h) \frac{\langle N_{total} \rangle}{\tilde{n}_g} b(M_h) \right]^2. \quad (13)$$

In Equations 12 and 13, $u(k|M_h)$ is the halo profile's mass-normalized Fourier transform; $P_m(k)$ is the matter power spectrum; \tilde{n}_g is the mean number density of galaxies given calculated as in Equation 9; and $b(M_h)$ is the scale-independent halo bias from Tinker et al. (2010).

From $\xi(r)$, we derive the angular correlation function within the `halomod` code (Murray et al. 2021) using the Limber's equation (Limber 1954) as presented in Blake et al. (2008):

$$w_{\text{halomod}}(\theta) = 2 \int_0^\infty dx f^2(x) \int_0^\infty du \xi(r = \sqrt{u^2 + x^2 \theta^2}) \quad (14)$$

$$f(x) = \frac{p(z)}{dx/dz(z)}, \quad (15)$$

where $p(z)$ is the redshift distribution which we deduce from the stacking of the individual galaxy's redshift probability density functions within a z -bin. x is the comoving radial distance from the median redshift, and $f(x)$ defines the overall radial distribution.

As mentioned in §3.1, the measured angular correlation function, $w_{\text{obs}}(\theta)$ is underestimated by a constant additive IC factor. Instead of adding this correction to $w_{\text{obs}}(\theta)$, we subtract it from $w_{\text{halomod}}(\theta)$ to get the model angular correlation function, $w_{\text{model}}(\theta)$, i.e. $w_{\text{model}}(\theta) = w_{\text{halomod}}(\theta) - \text{IC}$. We estimate IC as in Infante (1994) and Roche & Eales (1999):

$$\text{IC} = \frac{\sum_i w_{\text{halomod}}(\theta_i) RR(\theta_i)}{\sum_i RR(\theta_i)}, \quad (16)$$

where we run the θ_i out to much larger separations (~ 4 deg) than while measuring/modeling the angular correlation function itself (only out to ~ 0.25 deg) to ensure that we have counted all of the RR pairs. While fitting we can now compare $w_{\text{obs}}(\theta)$ and $w_{\text{model}}(\theta)$ directly (see §4.9) as both of them are lower by the same IC factor.

4.7. Stellar Mass Functions from the HOD

The SMF corresponding to a chosen set of HOD parameter values can be calculated using the occupation function and the HMF, dn/dM_h . Now, Equation 5 and

Equation 6 define the occupation functions with respect to a stellar mass threshold, however, the SMF is a series of values of number density per unit volume in bins of stellar mass. This means that we need the occupation function defined in bins of stellar masses instead of in thresholds of stellar mass. Fortunately, the occupation function within a stellar mass bin is simply the difference between the two stellar mass threshold-defined occupation functions at the mass thresholds $M_*^{t_1}$ and $M_*^{t_2}$ defining the bin edges:

$$\langle N(M_h|M_*^{t_1}, M_*^{t_2}) \rangle = \langle N(M_h|M_*^{t_1}) \rangle - \langle N(M_h|M_*^{t_2}) \rangle, \quad (17)$$

where, $\langle N \rangle$ represents the mean occupation function of the centrals, satellites, or total depending on whichever is desired. For a stellar mass bin defined by $\Delta \log_{10} M_* = M_*^{t_2} - M_*^{t_1}$, the modelled SMF, $\Phi_{\text{model}}(M_*^{t_1}, M_*^{t_2})$ can then be calculated as:

$$\Phi_{\text{model}}(M_*^{t_1}, M_*^{t_2}) \Delta \log_{10} M_* = \int_0^\infty \left(\langle N(M_h|M_*^{t_1}, M_*^{t_2}) \rangle \frac{dn}{dM_h} \right) dM_h, \quad (18)$$

where again $\langle N \rangle$ can be the mean occupation function of the centrals, satellites, or total depending on whichever SMF is desired.

4.8. Redshift evolution of the HOD parameters

As can be seen in Figure 2, the dynamical range in the stellar mass shrinks dramatically with redshift due to the widening range of incomplete stellar masses. The lowest stellar mass considered within the highest z -bin is $10^{10.3} M_\odot$ about 2 orders of magnitude higher than considered at the lowest z -bin. As a result, it becomes challenging to constrain the low-mass slope (controlled by β) of the SHMR at high- z . Due to the small dynamical range in stellar mass, the scatter in stellar mass at a fixed halo mass, $\sigma_{\log M_*}$ also proves harder to constrain.

Furthermore, even though the total effective survey area used in this study is large, it is not large enough to capture a high number of massive galaxies at all redshifts. Therefore, at all redshifts, it remains a struggle to constrain the δ and γ parameters which control the slope of the SHMR at the massive end and the transition regime between low-mass and high-mass, respectively.

This motivated us to consider an alternate approach to fitting the HODs. All of the 11 HOD parameters at each z -bin can be better constrained if it is realized that the clustering and SMFs in the neighboring z -bins are not disconnected from each other but rather evolve from one to another. Consequently, the HOD parameters that produce the clustering and abundance should also evolve smoothly, rather than having sharp jumps between the neighboring z -bins. We utilize this physically motivated

understanding by penalizing sharp changes in the HOD parameter values between the adjacent z -bins through the implementation of continuity (“smoothing”) priors.

Consequently, instead of fitting the clustering and abundance data for each of the individual z -bins (“discreet- z ” model hereafter), we jointly fit the data in all redshifts at once with the HOD evolving smoothly with redshift due to the continuity priors (“smooth- z ” model hereafter). This approach allows us to leverage the wealth of information contained within the clustering and abundance measurements at lower redshift spanning wider dynamical ranges in stellar mass, by connecting them to higher redshift via smooth redshift evolution of the HOD parameters.

To implement this smoothing, we use Gaussian priors that peak when there is no change in a given HOD parameter between the adjacent z -bins. For the HOD parameters that are fitted in log-space, $M_{*,0}$, M_1 , and $\sigma_{\log M_*}$, we impose the Gaussian continuity prior (centered at ‘0’) on the difference of the HOD parameter values between the adjacent z -bins, e.g. $\Delta \equiv M_1(z_x) - M_1(z_{x+1})$ as follows:

$$\text{prior}(\Delta) = \frac{e^{-\frac{1}{2}\left(\frac{\Delta}{\sigma}\right)^2}}{\sigma\sqrt{2\pi}} \quad (19)$$

where x denotes any x^{th} z -bin. Similarly, for all of the 8 other HOD parameters that are not fitted in log space, we impose the continuity prior (centered at ‘1’) on the ratio of the HOD parameter values between the adjacent z -bins, e.g. $\Delta \equiv \frac{\beta(z_x)}{\beta(z_{x+1})}$ as follows:

$$\text{prior}(\Delta) = \frac{e^{-\frac{1}{2}\left(\frac{\Delta-1}{\sigma}\right)^2}}{\sigma\sqrt{2\pi}} \quad (20)$$

where σ is the width of the Gaussian continuity prior decided such that the maximum range obtained with the “discreet- z ” fits is allowed to occur over the whole redshift range. Their values of σ along with the bounds on all the HOD parameters are tabulated in Table 2.

4.9. Fitting the HOD

Our primary results come from the “smooth- z ” model in which we jointly fit the HOD parameters at the 9 z -bins (described in 4.8) by minimizing the following χ^2 :

$$\chi^2 = \sum_z^Z \chi_w^2 + \chi_\Phi^2 \quad (21)$$

where

$$\chi_w^2 = \sum_i^{N_{M_*^t}} (\mathbf{w}_{obs, i} - \mathbf{w}_{model, i})^T \mathbf{C}_{obs, i}^{-1} (\mathbf{w}_{obs, i} - \mathbf{w}_{model, i}) \quad (22)$$

Table 2. σ of the gaussian priors on the change in HOD parameters between adjacent bins

HOD parameter	range	σ
$M_{*,0}$	10 – 12	0.065
M_1	11.8 – 14	0.12
β	0.1 – 0.9	0.06
δ	0.1 – 4	0.08
γ	0 – 8	0.12
$\sigma_{\log M_*}$	0.001 – 0.5	0.025
α_{sat}	0.4 – 2	0.07
β_{sat}	0.01 – 4	0.09
B_{sat}	0 – 17	0.065
β_{cut}	-1 – 8	0.145
B_{cut}	0 – 14	0.145

and

$$\chi_\Phi^2 = \sum_j^{N_{M_*^b}} \left(\frac{\log_{10}(\Phi_{obs, j}) - \log_{10}(\Phi_{model, j})}{\log_{10}(\sigma_{\Phi_{obs, j}})} \right)^2. \quad (23)$$

In Equation 22 above, the summing index i runs over $N_{M_*^t}$ stellar-mass threshold samples (shown in Table 1), and $\mathbf{C}_{obs, i}^{-1}$ is the inverse covariance matrix calculated using Equation 2. In Equation 23 the summing index j runs over $N_{M_*^b}$ stellar-mass bins used to evaluate the SMFs and $\sigma_{\Phi_{obs, j}}$ is the total error on the observed SMF, Φ_{obs} including contributions both from the Poisson statistics and the cosmic variance as described in §3.3. Finally, as we jointly fit all redshifts simultaneously, the index z in the outer sums in both terms runs over all the Z ($= 9$) z -bins.

In practice, we maximize the log-likelihood, $\ln(\mathcal{L}) = -\chi^2/2$ which is the same as minimizing the χ^2 using the python package `emcee` (Foreman-Mackey et al. 2013), which implements the affine-invariant Markov chain Monte Carlo (MCMC) ensemble sampler of Goodman & Weare (2010). As we jointly fit the HODs for all the z -bins, we have a total of 99 parameters = 11 HOD parameters at each z -bin \times 9 z -bins to be fit. We run 300 walkers to fit them until the resulting chains are converged. We consider the chains converged if they pass the typical convergence criteria that their auto-correlation time, τ (number of iterations before the chain ‘forgets’ where it started from) is at least 50 times smaller than the total number of iterations, and that the change in chains is less than $\sim 1\%$. After rejecting a certain number of iterations as ‘burn-in’, we retrieved the marginalized posterior distributions from the chains. The medians of the posteriors are considered the best-fit

values and the errors on them come from the 16th/84th percentiles.

To show the improvement in the HOD parameter fits due to the novel “smooth- z ” model, we also perform the HOD fitting in the standard way (“discreet- z ”) and compare the results in §5.2. For the “discreet- z ” model, the χ^2 formulation remains the same as in Equation 21 except for the outer sums running over all the z -bins which no longer apply. Furthermore, for the “discreet- z ” model as it fits each z -bin separately, we now only have 11 HOD parameters per fit. We fit them using 60 walkers until the chains are converged according to the same criteria as mentioned above.

5. RESULTS

5.1. Evolution of Clustering and Abundance

In Figure 4, we show our measurements (empty circles with error bars) of the two-point angular correlation function, $w_{obs}(\theta)$ for all of the stellar mass threshold sub-samples within each z -bin as defined in Table 1. The clustering of different stellar mass threshold samples is highlighted using different shades of the same color within each z -bin with darker shades representing higher mass thresholds as indicated in the legends. The strength of clustering increases with stellar mass on all scales which is unsurprising because more massive galaxies tend to reside in denser environments. We can also see a break from a power-law in the clustering amplitude between small scales and large scales due to the contributions from the pairs within the same halos at small scales (‘1-halo’) and from the pairs between different halos (‘2-halo’) at large scales as described in §4. In each panel, we highlight the scale where the ‘2-halo’ contribution to the real-space correlation function drops below that of ‘1-halo’ with a black marker. This break can be seen to be occurring at different scales in different z -bins because of how the co-moving transverse distance projected on the same angular scale on the sky changes with redshift due to the changing rate of expansion of the Universe.

The measured SMFs which are jointly fit with clustering to get the HODs are shown in the inset panels via filled circles and error bars. The evolution in SMF with redshift is also highlighted by the lowest z -bin SMF over-plotted as a dotted magenta curve in all the other panels. The lowest z -bin SMF has the characteristic ‘knee’ depicting a sharp drop in the number densities of the high-mass galaxies. This ‘knee’ is barely noticeable, if at all within the highest z -bin but gets more and more pronounced with decreasing redshift, indicative of increasing strength of feedback effects suppressing star formation in high-mass halos/galaxies (Silk & Rees 1998; Benson et al. 2003). Moreover, the steepening of the low mass slope with increasing redshift as reported in the literature (Davidzon et al. 2017; Weaver et al. 2023) can be seen. The over-plotted lowest z -bin SMF in all the other panels also highlights how the dynamic

range in stellar mass shrinks with redshift going from over 3 decades in stellar mass at $z \sim 0.35$ (lowest z -bin) to only about a decade at $z \sim 4$ (highest z -bin). This considerably weakens the SHMR constraining power of the high- z data (clustering+SMF) in isolation. However, the use of “smooth- z ” modeling in this paper connecting high- z with low- z using continuity priors remedies this to a large extent as shown in the following §5.2.

5.2. “Discreet- z ” vs. “smooth- z ” models

We introduced a novel approach to fitting the HOD model in §4.8 wherein we jointly fit clustering and SMF data within all of the 9 z -bins connected via smooth evolution (“smooth- z ” model) of the HOD parameters that produce the observed data.

In Figure 5, we show the increased constraining power of the “smooth- z ” model over the standard “discreet- z ” model in which the data in the individual z -bins are fitted with no regard to the adjacent z -bins. For each of the 11 HOD parameters, the yellow scatter points show the medians of the posteriors for the “discreet- z ” model, whereas the corresponding error bars show the range spanned by their 16th/84th percentiles. As hinted in §4.8, with the “discreet- z ” model, it proved a challenge to constrain the parameters sensitive to the data from the high stellar mass end of the SHMR at all redshifts and low-stellar mass end of the SHMR with increasing redshift.

At the high-mass end, it is the δ and γ that control the rise in the SHMR in the high-mass regime and the transition from low-mass to high-mass, respectively. Within most z -bins, the error-bars span a wide range within the bounds on $\delta \in [0.1, 4]$ and $\gamma \in [0, 8]$ meaning that they are very weakly constrained by the data when only considered one z -bin at a time. The weak constraining of the high-mass sensitive parameters δ and γ can be attributed to large uncertainties in the SMFs at the high-mass end (and the corresponding contributions to clustering) due to not capturing enough rare massive galaxies. Even though, our dataset covers a large effective survey area of $\sim 1.61 \text{ deg}^2$, pivotal in capturing a good number of rare massive galaxies, it is still not large enough to capture a large number of rare ultra-massive galaxies ($M_{*} \gtrsim 10^{11} M_{\odot}$) to pin down the SMF at the high mass end with confidence on par with the intermediate stellar masses. Therefore, it makes sense that the HOD parameters sensitive to the high-mass population, δ and γ cannot be constrained better, especially in the “discreet- z ” model.

At the low-mass end at high- z , it is challenging to constrain the β parameter, which controls the low-mass slope of the SHMR, due to the shrinking dynamical range in complete stellar masses with redshift. Moreover, at all redshifts due to the reasons mentioned above, the scatter in stellar mass at fixed halo mass, $\sigma_{\log M_{*}}$ also struggles to be constrained better than the accuracy of $\Delta \sim 0.1$ dex which remains unhelpful in informing the

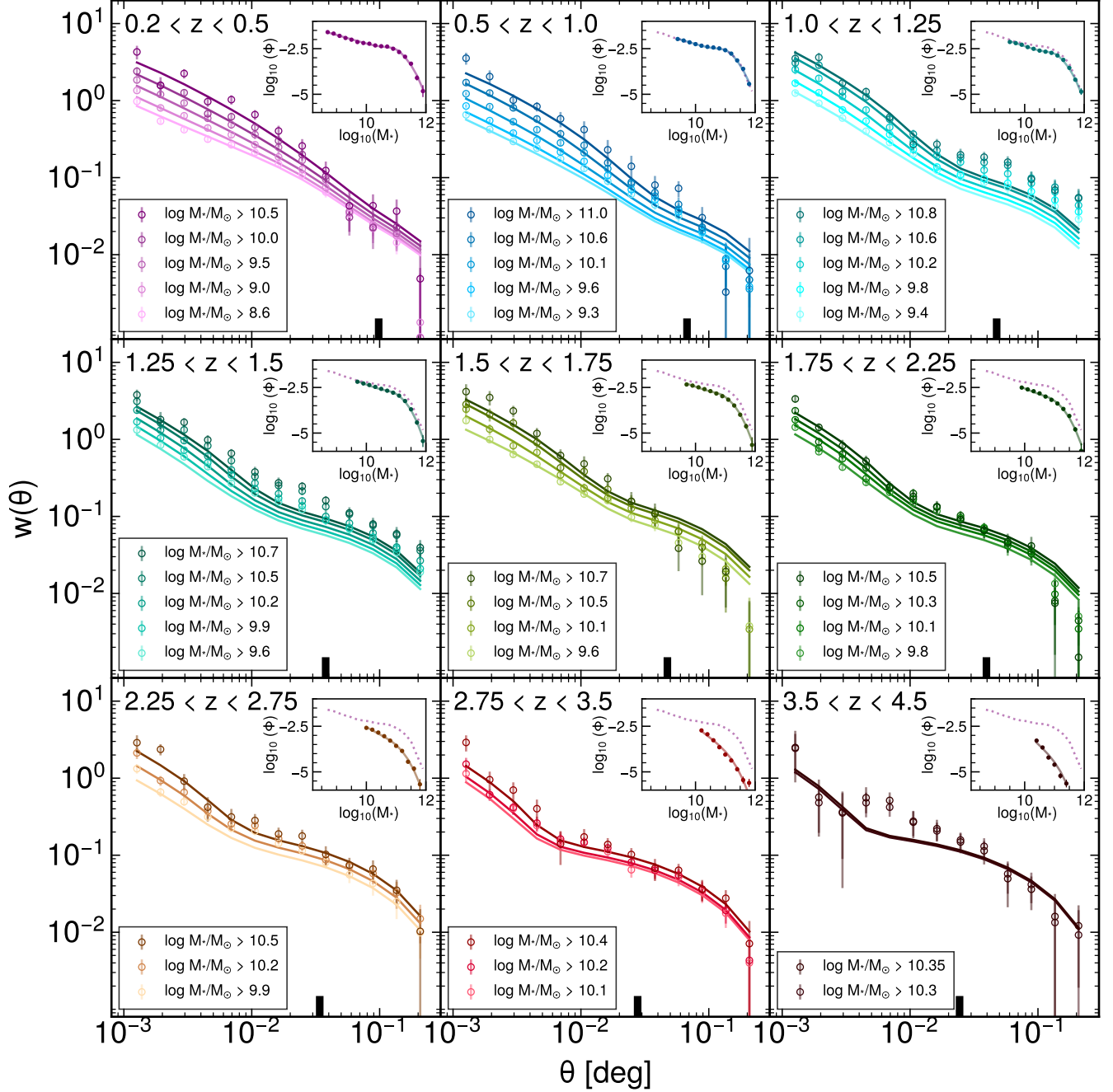


Figure 4. Clustering (main panels) and SMF (inset panels) measurements in the whole UDS+COSMOS sample along with the best fits of the “smooth- z ” model as a function of redshift. The empty circles in the main panels show the clustering measurements and their associated uncertainty, whereas the curves show the clustering produced by the best-fit model. Different mass threshold samples are indicated via color shading as indicated in the legends, with darker shades showing higher mass threshold samples. The breaks in scale, where the ‘2-halo’ contribution to $w(\theta)$ overtakes that of ‘1-halo’, are marked in black at the bottom of each panel. In the inset panels, the SMF measurements are shown via filled points and error-bars along with the curve going through them produced by the best-fit model.

strength of the stellar mass-halo mass connection. A small scatter would mean that the halo mass assembly is tightly linked to the stellar mass assembly in the Universe. In contrast, a large scatter would hint at the stel-

lar mass dependence on other halo properties beyond its mass, a possible indication of galaxy assembly bias perhaps. Therefore, it is crucial to constrain $\sigma_{\log M_*}$ better.

The “smooth- z ” model results are shown via the blue line (median) and the light blue shaded region (16th/84th percentiles) in Figure 5. The three HOD parameters that specially struggled to converge in the “discreet- z ” model as described above, are now remarkably well constrained at all redshifts.

Figure 6 shows that there are subtle differences between the clustering and SMF fits from the “discreet- z ” (left column in Figure 6) and “smooth- z ” (right column in Figure 6) models within the two highest z -bins. Yet the “smooth- z ” fits are a result of a much more physically motivated redshift evolution of the HOD parameters. Quantitatively, the reduced best-fit χ^2 for the “smooth- z ” fit, $\chi^2_{red,smooth-z} = 2.46$, where the degrees of freedom, $DOF = 472 = 571$ (# of data points within all z -bins) - 99 (11 \times 9 HOD parameters within all z -bins). Within “discreet- z ” model, if we add all the raw best-fit χ^2 from the individual z -bin fits, we can then divide the total by the same DOF as in “smooth- z ”, to get $\chi^2_{red,discreet-z} = 2.13$, which can be compared directly to $\chi^2_{red,smooth-z}$.

5.3. Redshift evolution of the mean SHMR for centrals

The fitted SHMR at each z -bin also allows us to paint a continuous picture of the evolution of SFE from $z = 4.5$ to $z = 0.2$. Using the median fitted values of the central HOD parameters in equation 3 at each redshift, we plot the stellar-halo mass ratios (M_*/M_h) as a function of the halo mass in each panel of Figure 7. To highlight the redshift evolution in M_*/M_h , we also show the M_*/M_h of the lowest z -bin (in magenta) in the rest of the panels. The M_*/M_h of a halo directly indicates how efficient the halo has been, throughout its lifetime, in converting baryonic matter into stellar matter. The SFE, given by dividing M_*/M_h by the baryonic fraction of the universe, $f_b = 15.8\%$ (Planck Collaboration et al. 2020), is indicated on the right in Figure 7.

Furthermore, the halo mass regimes not directly probed by our data, both at low-mass and high-mass end, are shaded in gray. The lowest halo mass probed is given by the mean central SHMR at the lowest stellar mass threshold within each z -bin. On the other side, the highest halo mass probed is considered where the mean number of galaxies (derived using the fitted HOD at the respective redshift) drops below 0.6 within the volume covered.

The low-mass slope starts relatively flat in the highest z -bins and steepens the most through the $2.25 < z < 2.75$ (7th) and $1.75 < z < 2.25$ (6th) z -bins. This is also evident in the decrease in β with decreasing redshift seen in Figure 5; higher values indicate flatter slopes. At the low mass end, smaller-scale feedback effects such as

supernovae, stellar winds, etc. are thought to heat up or expel their surrounding gas and suppress star formation (Hopkins et al. 2012). Therefore, the redshift evolution of the low-mass slope hints at the strengthening of such feedback effects with time.

On the other hand, $M_{*,meancen}/M_h$ declines at the high-mass end at all redshifts. The active galactic nuclei (AGN) feedback is purported to be responsible for curbing star formation in massive galaxies (Silk & Rees 1998; Benson et al. 2003), predominantly in ‘jet-mode’ (Silk & Rees 1998; Croton et al. 2006; Kondapally et al. 2023; Scharré et al. 2024), explaining the decline in $M_{*,meancen}/M_h$ at the high mass end. Moreover, the high-mass slope remains remarkably consistent throughout the z -bins. This indicates that the strength of AGN feedback beyond the peak halo mass is strongly coupled to the halo mass and depends weakly, if at all, on the age of the Universe.

The combination of the low and high-mass slopes result in a narrow range in halo mass for peak star formation at each redshift, $M_h^{peak} \sim 10^{12.2} - 10^{12.4} M_\odot$, reflecting SFE $\sim 13 - 20\%$. This value of $M_h^{peak} \sim 10^{12} M_\odot$ is well supported by a series of observational studies (Behroozi et al. 2013, 2019; Ishikawa et al. 2017; Cowley et al. 2018; Moster et al. 2018; Shuntov et al. 2022). It is important to note that even though the adopted L11 model allows for a transition regime between low mass and high mass, it does not necessitate a peak halo mass; it naturally comes out of the fitting.

5.4. Redshift evolution of the peak halo mass, M_h^{peak}

To better understand the evolution of the feedback effects suppressing star formation, we now look at the evolution of the halo mass with *peak* integrated SFE, M_h^{peak} in Figure 8. M_h^{peak} are the peaks in Figure 7. Using the combined sample (UDS+COSMOS), we show the evolution of M_h^{peak} in Figure 8 using a black line, with the gray shaded region showing the 1σ uncertainty evaluated using the MCMC chains. We also show a compilation of results from the literature indicating the method they used to derive M_h^{peak} in the legend, whether it was empirical modeling (emp), abundance matching (AM), or HOD like in our case. In our case, there is a *downtuning* (Cowie et al. 1996) trend since $z = 1.5$, meaning that the most efficient halo mass (M_h^{peak}) declines from $10^{12.37^{+0.03}_{-0.03}} M_\odot$ at $z \sim 1.4$ to $10^{12.22^{+0.03}_{-0.04}} M_\odot$ in the lowest z -bin ($z \sim 0.35$), exhibiting a decline of 0.11 dex. Beyond $z = 1.5$, M_h^{peak} is consistent with no evolution, within the errors. The overall weak evolution in M_h^{peak} with redshift shows that halo mass assembly in halos is tightly linked to the stellar mass assembly.

The relatively small error (0.2–0.3 dex) on M_h^{peak} within the highest two z -bins ($2.75 < z < 4.5$) can be attributed to the new “smooth- z ” model (introduced in §4.8) used in this study. This model, which connects

³ the $\chi^2_{red,discreet-z}$ calculated using the median models is actually larger since some parameters are so poorly constrained in high z -bins that the median is not that close to the best fit

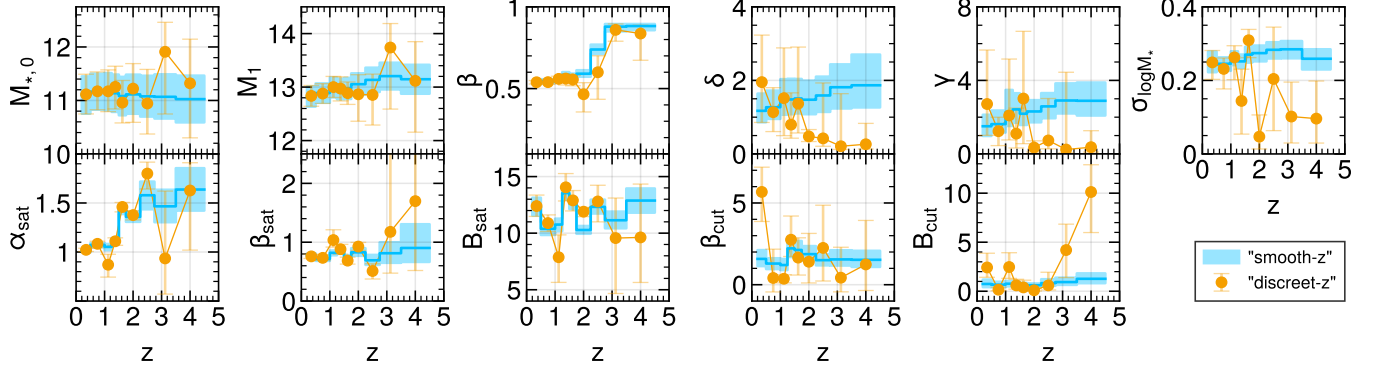


Figure 5. HOD parameter fits derived through the “discreet- z ” model are shown in yellow scatter points and the ones derived using the novel “smooth- z ” model are shown via the blue line. The errors indicated through yellow bars for “discreet- z ” and blue-shaded envelope for “smooth- z ” encompass the posteriors’ 16 – 84 percentile range.

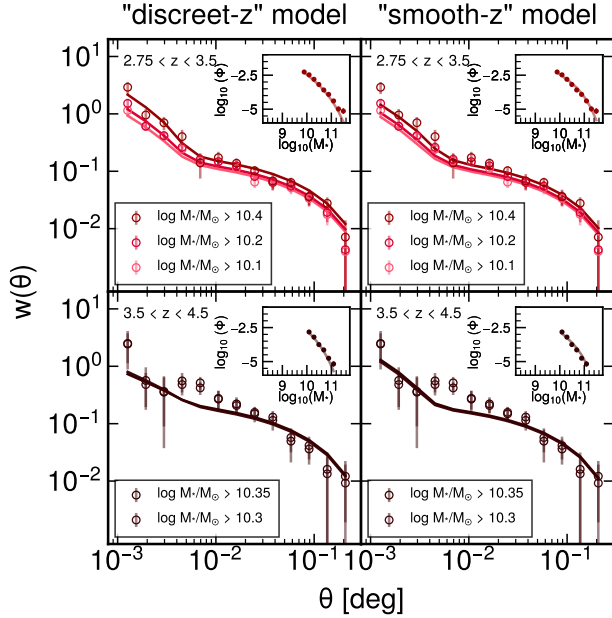


Figure 6. Clustering and SMF fits using the “discreet- z ” model (left column) vs. the “smooth- z ” model (right column) of the two highest z -bins.

the HOD parameters at low- z and high- z discouraging any unphysical inter- z -bin ‘jumps’, leverages the high constraining power of the low- z data with a much wider dynamical range in stellar mass than at high- z . As a result, we could shrink the uncertainty on $\log_{10}(M_h^{peak} [M_\odot])$ at high- z by up to a factor of ~ 6.5 compared to Shuntov et al. (2022), who applied the same HOD (L11) as we did on a similarly large effective area of $\sim 1.27 \text{ deg}^2$, but fitted the individual z -bins separately. Furthermore, we reduced the impact of uncertainties due to cosmic variance by utilizing two large fields (total effective area $\sim 1.61 \text{ deg}^2$) instead of one.

Overall, our results generally agree with the observationally constrained M_h^{peak} in the literature as can

be seen in Figure 8. However, at $z < 1.5$, where the wider dynamical range in stellar masses, than at higher redshifts, provides stronger constraining power for all studies, there seems to be a systematic offset between our M_h^{peak} and others’: Our M_h^{peak} remains consistently higher by ~ 0.10 – 0.15 dex at $z < 1.5$. We checked if this discrepancy washes away using the stellar masses from derived using FAST instead of Dense Basis, but that is not the case: At $z < 1.5$, M_h^{peak} values derived using the stellar masses from the two codes have a median offset of ~ 0.018 and a mean offset of 0.006. Below, we further delve into our investigation of this systematic discrepancy.

5.4.1. Effect of cosmic variance on the redshift evolution of the peak halo mass at $z < 1.5$

All of the previous M_h^{peak} results in the literature at these redshifts are based either purely on the COSMOS field (Leauthaud et al. 2012; Cowley et al. 2018; Legrand et al. 2019; Weaver et al. 2022) or rely heavily on the COSMOS field despite having data from other fields in the case of Behroozi et al. (2019)⁴ and Moster et al. (2018).

One of the key advantages of this work is the introduction of the UDS as second field. This difference seems a likely explanation for the offset in our $z < 1.5$ M_h^{peak} results from those in the literature. To test this possibility we reanalyzed the data from COSMOS and UDS fields alone to see if our COSMOS-only M_h^{peak} agrees with the

⁴ Besides COSMOS-based SMFs, at $0.05 < z < 1$, Behroozi et al. (2019) utilize the SMFs from Moustakas et al. (2013) which is based on 5 PRIMUS fields (CDFs, COSMOS, ELAIS-S1, XMM-SXDS, XMM-CFHTLS) covering a large total area of 5.5 deg^2 . However, due to the photometry problems in Moustakas et al. (2013) as discussed in the appendix (C2) of Behroozi et al. (2019), they exclude the constraints from Moustakas et al. (2013) on the massive end ($M_* > 10^{11} M_\odot$) beyond $z > 0.2$. This is also the mass regime where the COSMOS SMF deviates the most from UDS SMF (COSMOS SMF is much over-dense) as shown in Fig. 9.

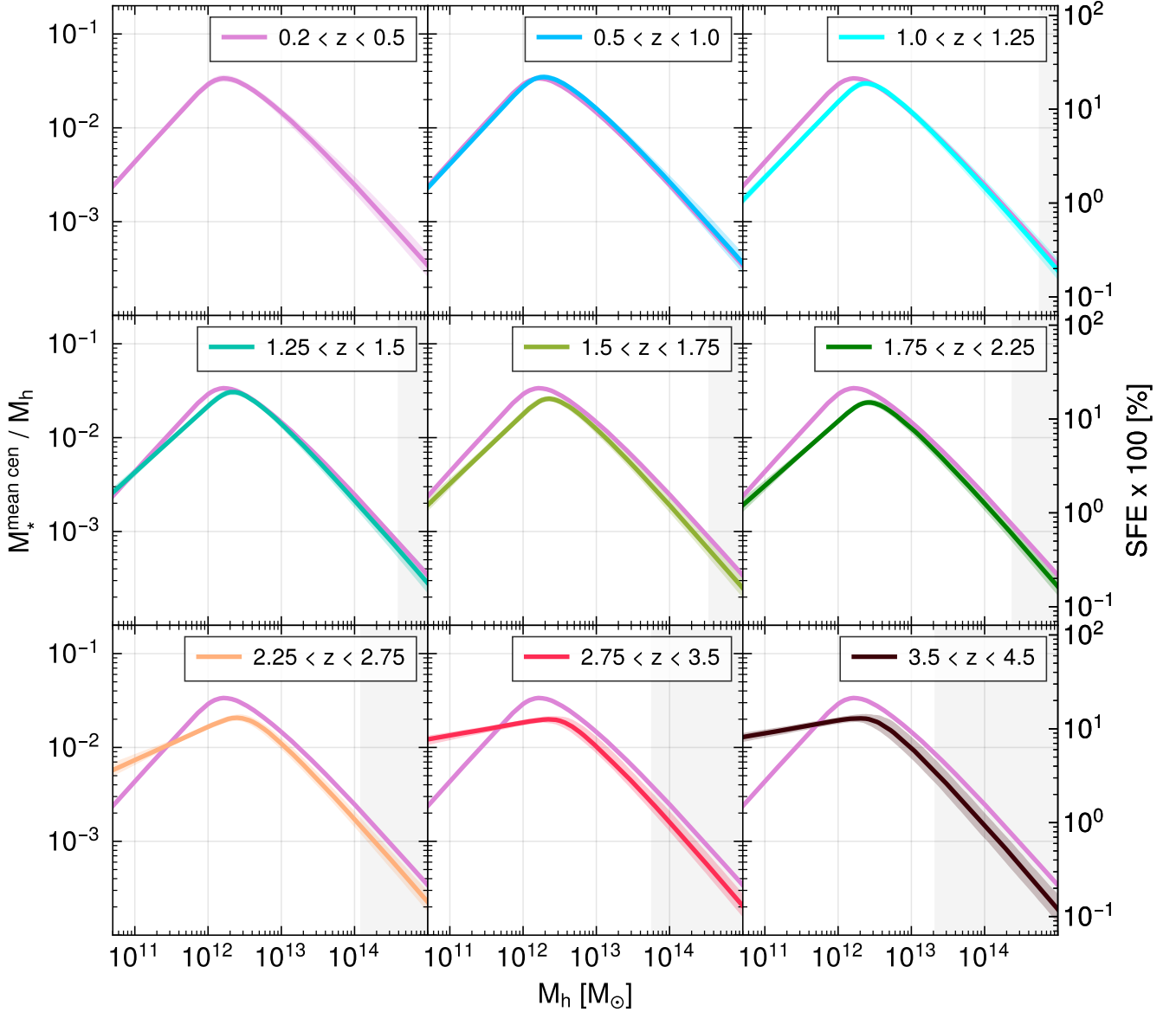


Figure 7. Mean stellar-to-halo mass ratio of central galaxies, $M_{*,\text{mean cen}}/M_h$ as a function of halo mass for each z -bin shown in each panel. The magenta curve showing the $M_{*,\text{mean cen}}/M_h$ for the first z -bin is over-plotted in all the other panels to highlight the overall evolution in $M_{*,\text{mean cen}}/M_h$ since $z \sim 4.5$. The SFE ($= (M_{*,\text{mean cen}}/M_h)/f_b$) in percentages is indicated on the right-most ordinate. The gray shaded regions represent halo masses not directly probed in our analysis, as described in §5.3.

literature. If the M_h^{peak} resulting from the clustering and SMF measurements in our COSMOS dataset fitted with the HOD model agreed well with the COSMOS-dominated results in the literature, it would be a clear indication that our UDS+COSMOS M_h^{peak} is driven upward due to the addition of UDS field. This is exactly what we see in Figure 8, where our COSMOS-only M_h^{peak} results, shown with the black ‘+’, lie almost exactly atop the M_h^{peak} points from other studies. Our UDS-only M_h^{peak} results shown with the black ‘x’ are much

higher, which as speculated, drives the UDS+COSMOS M_h^{peak} upward compared to the COSMOS-only case.

We delved further into the cause of these field to field differences in the clustering and SMF in Figure 9. In the left part of the figure, we show the clustering offsets for the lowest and highest mass threshold samples within each of our four z -bins out to $z = 1.5$. Clustering does not change significantly between the two fields except for the highest mass threshold ($M_* > 10^{11}M_\odot$) sample at $0.5 < z < 1.0$. Therefore, it is hard to infer any resulting change on M_h^{peak} .

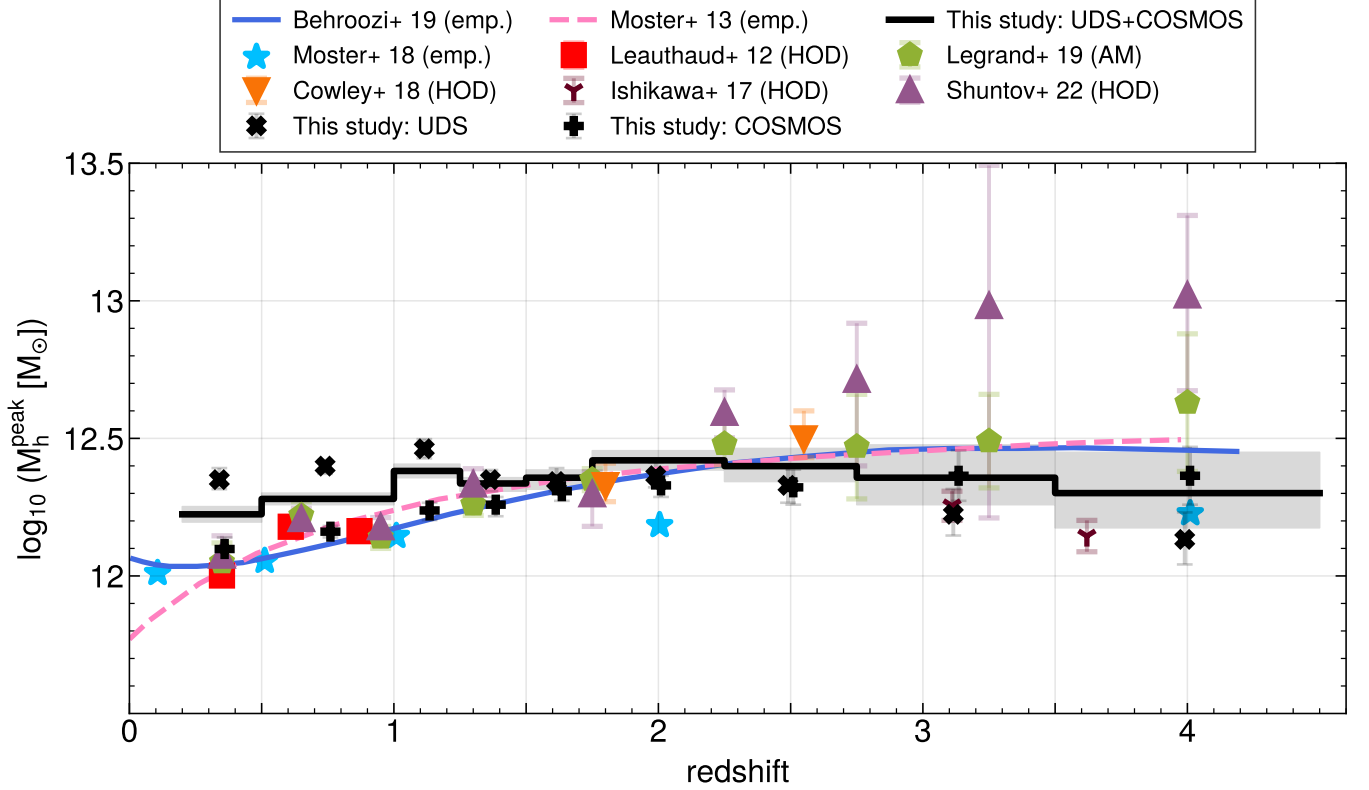


Figure 8. Redshift evolution of the halo mass, M_h^{peak} at which the $M_*^{mean\ cen}/M_h$ ratio as shown in Figure 7 peaks representing the peak SFE (integrated over halo’s lifetime). The black line and the gray shaded region shows our main result and the corresponding 1σ uncertainty, respectively, derived using the full UDS+COSMOS sample. We also indicate the median M_h^{peak} and 1σ errors using only UDS (black \times ’s) and COSMOS (black $+$ ’s), highlighting the effect of cosmic variance. A compilation of other observationally constrained M_h^{peak} values in the literature using different methods - Abundance matching (AM), empirical modeling (emp), and HOD modeling, as in our case, are also shown.

However, the SMF offset shown in the right part of Figure 9 shows that the COSMOS SMFs are systematically over-dense (higher normalization) for most of the stellar masses out to $z = 1.5$. Below, we elaborate on the convincing evidence for the generally over-dense nature of the COSMOS SMF compared to the UDS SMF:

- $0.2 < z < 0.5$: At $M_* \gtrsim 10^{9.2} M_\odot$, the COSMOS SMF offset remains consistently over-dense by $\sim 0.1-0.2$ dex, except for the high-mass end, where the offset diminishes within errors.
- $0.5 < z < 1.0$: At $M_* \gtrsim 10^{10} M_\odot$, the COSMOS SMF is again over-dense by ~ 0.2 dex until $M_* \sim 10^{11.2} M_\odot$, beyond which it abruptly increases in over-density to reach an offset of ~ 1 dex at $M_* \sim 10^{11.8} M_\odot$.
- $1.0 < z < 1.25$: At $M_* \sim 10^{10.3} M_\odot$, the COSMOS SMF starts to become over-dense steadily until $M_* \sim 10^{11.5}$, before rising sharply to reach an offset of ~ 1.1 dex at $M_* \sim 10^{11.7} M_\odot$.
- $1.25 < z < 1.5$: Only at $M_* \gtrsim 10^{10.9} M_\odot$, the COSMOS SMF starts to become over-dense, steadily reaching a maximum offset of ~ 0.3 dex at $M_* \sim 10^{11.5} M_\odot$.

COSMOS is found to be under-dense than UDS only within $1.0 < z < 1.25$ and $1.25 < z < 1.5$ bins at inter-

mediate masses at $M_* \lesssim 10^{9.9} M_\odot$ and $M_* \lesssim 10^{10.3} M_\odot$, respectively.

The over-dense nature of COSMOS is not surprising as several massive structures, out of which five are $M_* > 10^{13} M_\odot$ have long been reported (Scoville et al. 2007b) in the field at $z < 1.1$. There is a super-structure at $z \sim 0.8-0.9$ (Darvish et al. 2014). McLeod et al. (2021) have also shown that UDS SMFs are less dense than COSMOS SMFs at $0.25 \leq z < 1.25$.

The effect this has on our HOD-modeling-derived M_h^{peak} can be understood by considering the SMFs and the adopted HMF. Due to the higher normalization of COSMOS, more galaxies need to be assigned to halos. The additional galaxies in COSMOS can be accommodated in two ways: (i) be hosted as satellites in high mass halos, thus increasing the slope of satellite occupation function, α_{sat} , OR (ii) by decreasing the halo mass cutoff to host central galaxies, which allows less massive halos to also host galaxies.

According to the first way, the clustering should increase on all scales but we do not see that in Figure 9. Therefore, the second option is more likely - the halo

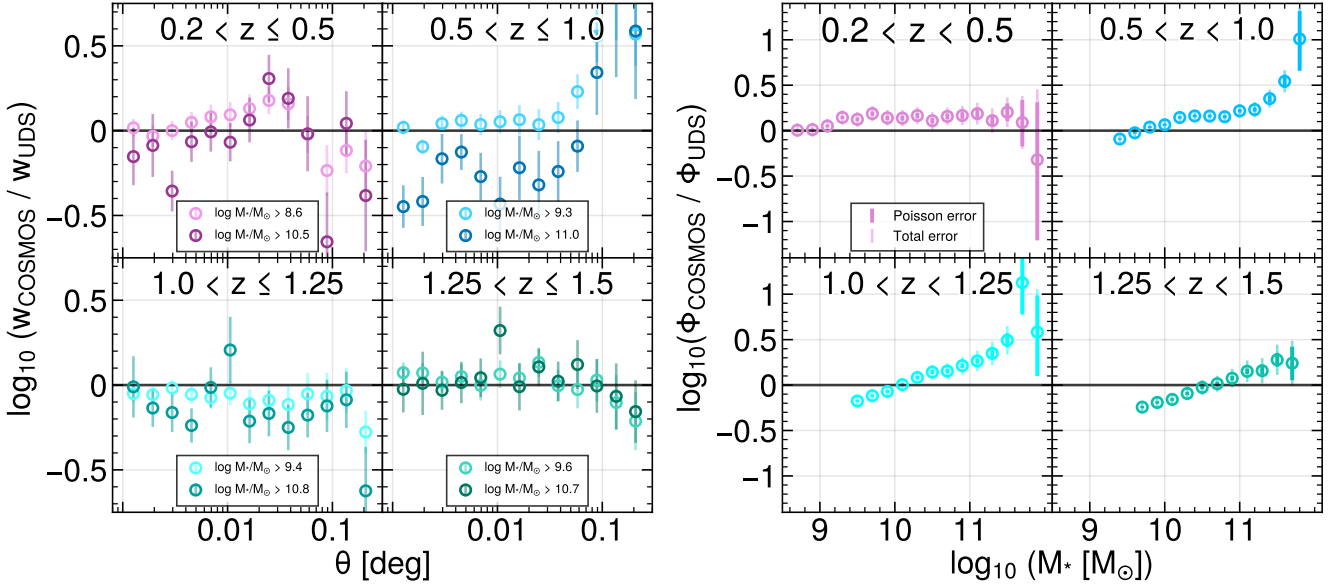


Figure 9. Left: Measured clustering offsets between the UDS and COSMOS fields at $z < 1.5$. Each of the four panels (four z -bins as indicated at each panel’s top) shows the offset in the two-point angular correlation functions corrected for integral constraints. Within each panel (z -bin), the offset is shown for the lowest and the highest stellar mass threshold samples (as described in Table 1) with the legend indicating the thresholds. **Right:** Measured SMF offsets between the UDS and COSMOS fields in the four z -bins indicated at each panel’s top. Here, we highlight the error budget attributed to Poisson with thicker error bars, whereas the total error including the cosmic variance (CV) is shown with thinner error bars.

mass cutoff to host central galaxies lowers to accommodate more galaxies as centrals in COSMOS. Inevitably, this lowers the average halo mass essentially captured by the characteristic halo mass, the M_1 parameter in the L11 HOD. Since M_1 in COSMOS is lower, the effect of which is to shift the SHMR leftwards (towards lower halo masses), the M_h^{peak} also shifts to lower halo masses as we see in Figure 8.

We see a clear signature of the effect of the SMFs requiring the HOD to put galaxies at lower halo masses in these z ranges in Figure 4. The best fit $w(\theta)$ models are all offset systematically low compared to the data in the $1.0 < z < 1.25$ and the $1.25 < z < 1.5$ bins, particularly on large scales.

5.5. Redshift evolution of the total (central+satellite) SHMR

Beyond halo masses of about $\sim 10^{12.5} M_\odot$, depending on redshift, the contribution of satellites to the total stellar mass budget of the halo starts to become noticeable. The L11 HOD model used in this study allows us to easily calculate the contribution of central and satellites to the total stellar mass locked up in a halo of a given mass through Equation 10, where we essentially integrate the conditional SMF down to a lower limit on stellar mass.

Similar to Leauthaud et al. (2012) and Shuntov et al. (2022), we integrate down to a stellar mass, $M_* = 10^9 M_\odot$ and show the resulting total stellar-to-halo mass ratios, M_*^{tot}/M_h (solid curves) split between cen-

trals (dashed curves) and satellites (dash-dotted curves) in Figure 10. We also estimate the 1σ errors on $M_{*,total}/M_h$ using the MCMC samples and show them as shaded regions. Furthermore, as in Figure 7 (and described in §5.3), we shade the halo masses not directly probed in our analysis in gray.

Below $M_h \sim 10^{12} M_\odot$, the satellite contribution remains subdominant compared to the central galaxy. Beyond $M_h \sim 10^{12} M_\odot$, the central galaxies account for a smaller and smaller fraction of the total stellar mass in halos, and the satellites take over beyond $M_h \sim 10^{13.6} M_\odot$ (group/cluster scale halos), with a slight dependence on redshift. Interestingly, within the halo masses probed, the peak total SHMR is dictated almost entirely by centrals and occurs around the M_h^{peak} values in §5.4 ($\sim 10^{12.3} M_\odot$). This is unsurprising as M_h^{peak} just represents the peak of $M_*^{mean cen}/M_h$ which is the mean of $M_*^{total cen}/M_h$.

Although, beyond $M_h \sim 10^{13} M_\odot$ at $z > 1.5$, there is a hint of an upturn in M_*^{tot}/M_h which could be due to satellites on their way to merge with the central galaxy. M_*^{tot}/M_h also rises in the 2nd z -bin ($z \sim 0.75$) relative to the 3rd z -bin ($z \sim 1.1$), and then falls back again in the lowest z -bin ($z \sim 0.35$). This indicates that at $z \sim 0.75$, there is an uptick in the satellite accretion onto the most massive galaxies, and by $z \sim 0.35$ those satellites have mostly merged with the massive central galaxies. We discuss this in §6.2 as well.

So far for these total stellar mass calculations we have used a lower stellar mass limit of the integration of $M_* = 10^9 M_\odot$. Ideally, we would like to extend the lower limit down to dwarf galaxies ($10^7 - 10^8 M_\odot$) and it is possible to extrapolate our fitted HOD models to such low stellar masses. However, our data does not provide constraints below the stellar mass completeness limit, which is already above $10^9 M_\odot$ for all but our lowest redshift samples. However, as has previously been noted (Leauthaud et al. 2012; Shuntov et al. 2022), as long as the low mass slope of the satellite conditional mass function (Figure 11) is sufficiently shallow, lowering the integration limit does not change the satellite contribution significantly. This is the case for all but our highest z -bin.

5.6. Redshift evolution of the SMFs for halos with fixed masses

We derive the conditional (on halo mass) SMFs for our best-fit models by adjusting the integration limits in Equation 18. The SMFs of 0.5 dex wide halo mass bins from $10^{11.5} - 10^{13.5} M_\odot$ are shown in Figure 11, with the legend at the top indicating the four halo mass bins. The contributions from centrals and satellites are shown separately through dashed and solid curves, respectively, and the shaded regions represent the 1σ uncertainties. The central galaxies see a tight correlation with all halo mass bins out to $z = 4.5$; their SMF peak at a certain stellar mass which increases with halo mass, and falls off abruptly on either end. This tight correlation of centrals with halo mass is not enforced by HOD modeling, as we fitted for the scatter in stellar mass at fixed halo mass, $\sigma_{\log M_*}$ which is linked to the scatter in M_h at fixed M_* , $\sigma_{\log M_h}$ relevant here. As described in L11, since the SHMR behaves like a power law at low-mass, $\sigma_{\log M_h} = \beta \times \sigma_{\log M_*}$, where β controls the low-mass slope. At high-mass, $\sigma_{\log M_h}$ rises at a rate set by δ and γ . In our fits, $\sigma_{\log M_*}$ was allowed to reach 0.5 dex, i.e. $\sigma_{\log M_*} \in [0.001, 0.5]$, but it never surpassed ~ 0.3 dex in any z -bin, indicating that the tight correlation of centrals with M_h we observe was not enforced via HOD modeling.

On the other hand, satellites have huge scatter; there is almost no preference for the halo mass for satellites less massive than $M_* \sim 10^{10} M_\odot$. This highlights how simple abundance matching by rank ordering halos and galaxies with mass is not enough. Clustering provides additional information which can then be used to constrain the contribution of number densities to central and satellite galaxies individually. Satellites more massive than $M_* \gtrsim 10^{10} M_\odot$ are naturally hosted according to their mass; more massive satellites reside in more massive halos hierarchically.

5.7. Redshift evolution of the satellite fractions

As shown in §5.5, satellites start to contribute noticeably to the stellar mass budget of the halos beyond $M_h \sim 10^{12} M_\odot$. Their contributions continue to rise and

end up dominating the stellar mass budget beyond $M_h \sim 10^{13} M_\odot$ in the group and cluster-scale halos. As satellites are acquired through mergers, analyzing the redshift evolution of satellite fraction, f_{sat} (calculated using Equation 9) can shed light on the evolution of the environment of these halos.

In Figure 12, we show the stellar mass threshold dependence of f_{sat} in bins of redshift (left panel) as well as the redshift dependence of f_{sat} for different stellar mass thresholds (right panel). Within each z -bin at, f_{sat} only weakly grows as the stellar mass threshold is lowered to include more and more galaxies. For instance, in the $1.0 < z < 1.25$ bin (shown in cyan), f_{sat} only evolves from $\sim 19\%$ to 23% . Indeed at any redshift, lowering the stellar mass threshold does not increase the f_{sat} by more than $\sim 7\%$ within the stellar mass ranges considered. Furthermore, even within the lowest z -bin with the lowest stellar mass threshold ($M_* > 10^{8.7} M_\odot$) considered here, where f_{sat} is maximized as expected, it only reaches $\sim 30\%$.

The plateauing of f_{sat} with decreasing stellar mass threshold, visible at $z < 1$, can be attributed to the much higher abundance of the low-mass halos and the sharp decline at the high-mass end of the HMF. Therefore, as the stellar mass threshold is lowered to include more and more low-mass galaxies, they are more likely to be allocated as central galaxies in highly abundant low-mass halos than as satellites in rare high-mass halos. Even though the occupation number of satellites increases as a power law as halo mass increases, due to the shape of the HMF, there are just too few high-mass halos available to host many low-mass satellites. Therefore, low-mass galaxies are more often hosted as centrals in low-mass halos (Shuntov et al. 2022).

While the dependence of f_{sat} on stellar mass threshold is relatively weak, it depends much more strongly on redshift such that it increases sharply as the Universe ages as seen by the vertical offsets between different z -bins again in the left panel of Figure 12. This is shown more clearly in the right panel of Figure 12, where f_{sat} sees an overall increasing trend with decreasing redshift, and plateaus at $z \lesssim 0.75$. In general, at each redshift, the lower the stellar mass threshold, the higher its f_{sat} , unsurprisingly.

5.8. Redshift evolution of the M_*^{tot}/M_h at fixed halo masses

We present the evolution of M_*^{tot}/M_h (or integrated SFE) in halos of fixed masses - $M_h^{peak}(z)$, $10^{11.5}$, 10^{12} , $10^{12.5}$, and $10^{13.5} M_\odot$ in Figure 13. $M_h^{peak}(z)$ halos are always the most efficient by definition which closely trace the $10^{12.5} M_\odot$ halos (in red) indicating that the M_h^{peak} does not deviate much from $\sim 10^{12.5} M_\odot$ with redshift, as already described in §5.4. At $z < 2$, the slightly lower $M_h = 10^{12} M_\odot$ (in green), and the lowest $M_h = 10^{11.5} M_\odot$ (in blue), continue to rise in SFE with

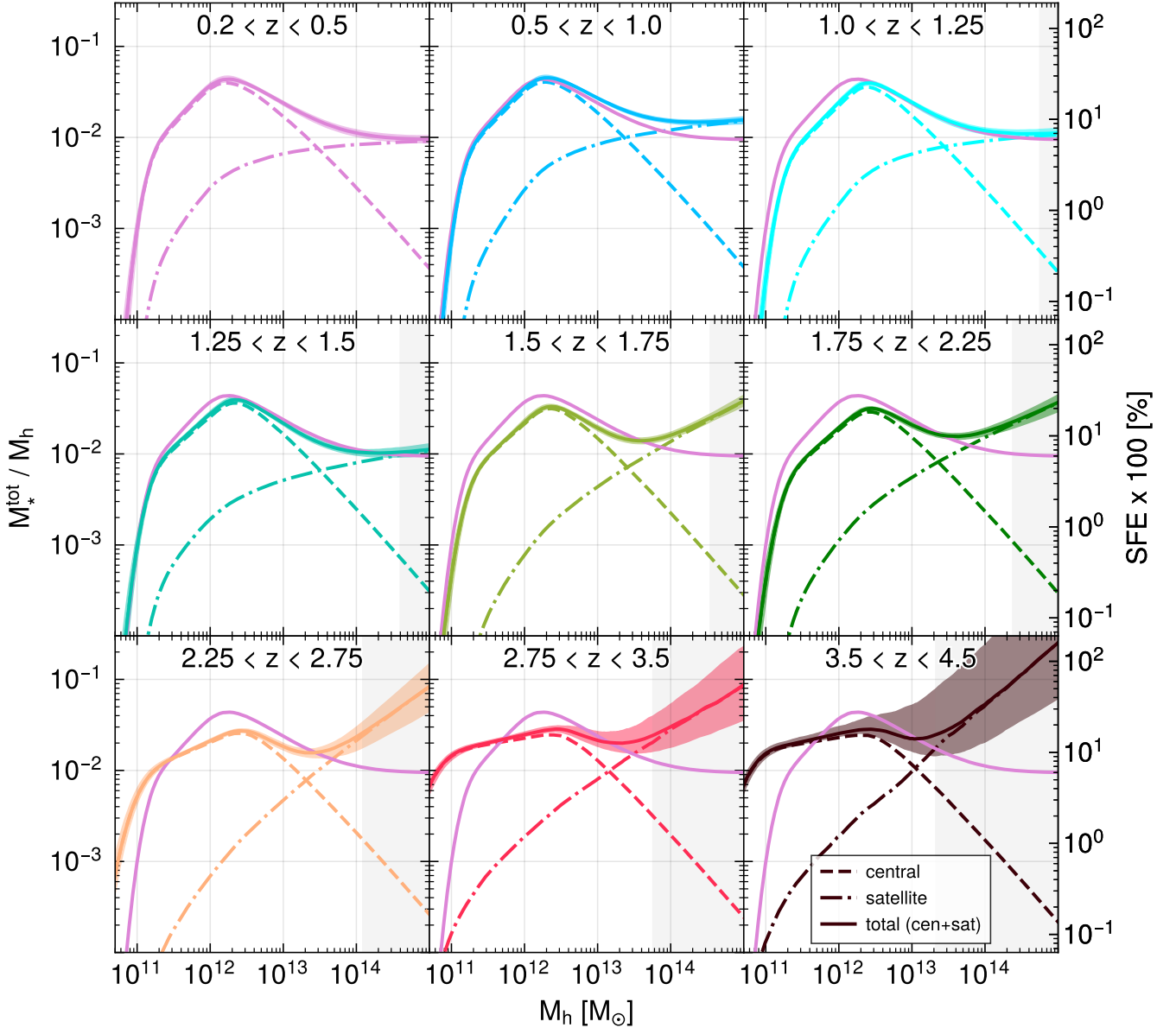


Figure 10. Total (central+satellites) stellar mass locked up in halos divided by the halo mass, $M_{*,total}/M_h$ ratio as a function of halo mass within each z -bin (each panel). The solid-colored curve shows the median $M_{*,total}/M_h$ and the shaded envelope shows encapsulates $1\text{-}\sigma$ error. The dashed curves show the contribution of central galaxies to the $M_{*,total}/M_h$, whereas the dot-dashed curves show the contribution from satellite galaxies. The magenta-colored curve showing the $M_{*,total}/M_h$ of the first z -bin (top-left panel) is over-plotted in all the other panels to highlight its evolution with redshift. As in Figure 7, the right-most ordinate indicates the SFE ($= (M_*^{\text{mean cen}}/M_h)/f_b$) in percentage. The gray shaded regions indicate the halo masses not directly probed in our analysis, as in Figure 7.

decreasing redshift. However, both remain consistently lower in SFE than the $M_h = 10^{12.5}M_\odot$ (or M_h^{peak}) halos by factors of ~ 1.5 and ~ 4 , respectively.

On the other side of M_h^{peak} , at $M_h = 10^{13.5}M_\odot$ (in yellow), a reverse trend is seen where the SFE continues to decrease with decreasing redshift (barring a slight uptick at $z \sim 0.75$), indicating that the high mass ha-

los do bulk of their star formation early on and become more and more quiescent over time.

5.9. Redshift evolution of SHMR along the halo merger trees

So far in this paper, halo masses or SHMR (total or otherwise) have been inferred from HOD fitting of large samples of galaxies in fixed z -bins. We have then made

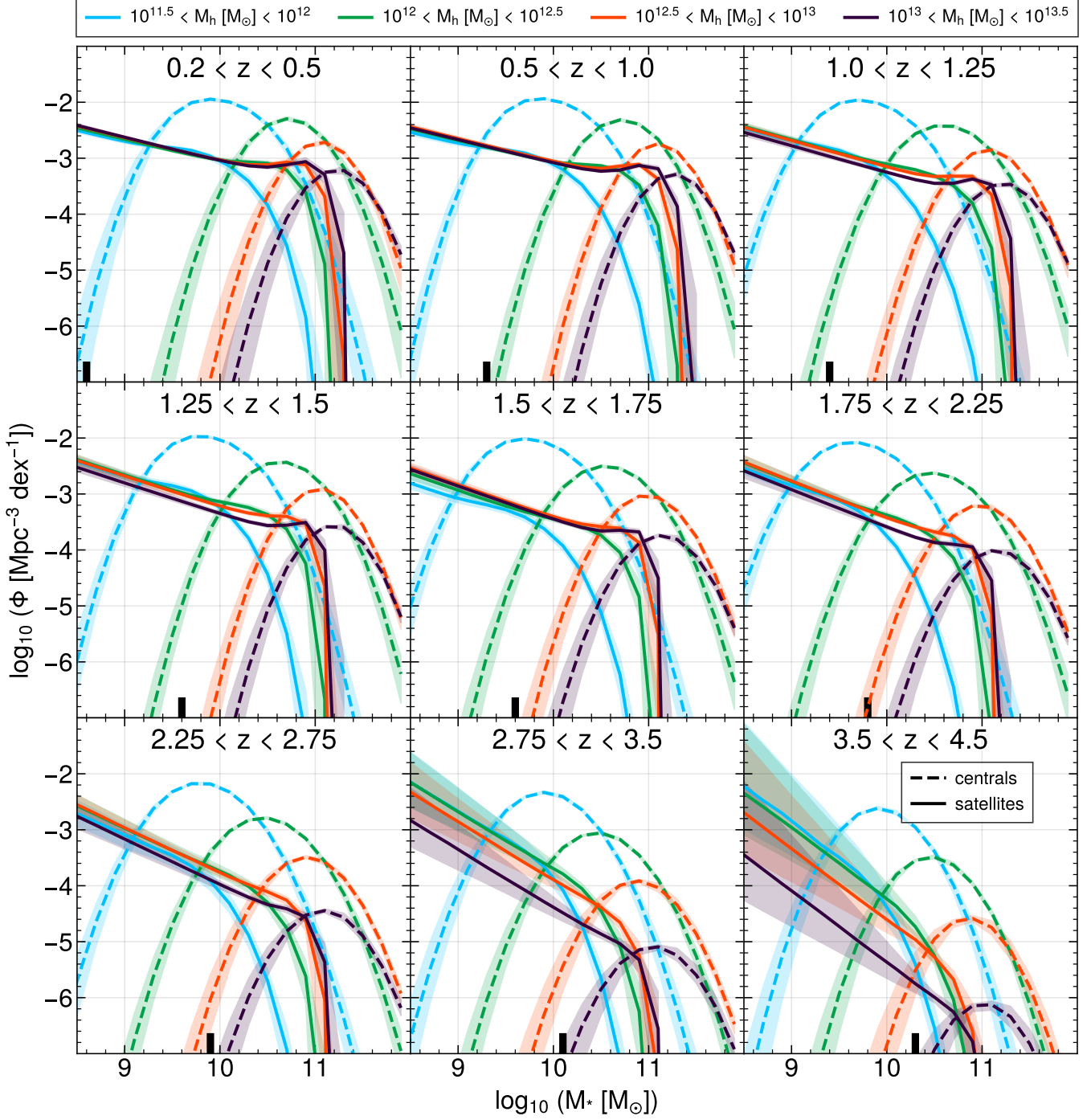


Figure 11. SMFs for centrals (dashed curves) and satellites (solid curves) within 0.5 dex wide bins of halo masses highlighted in different colors and indicated in the legend. The lowest stellar mass threshold considered within each z -bin, due to the stellar mass completeness (as described in §2.2 and quoted in Table 1) is indicated with a black marker at the bottom of each panel.

comparisons of the evolution of various galaxy and halo properties with redshift either at fixed galaxy or halo mass. However, galaxies and halos are both evolving in mass with redshift and so by comparing at fixed mass we are not comparing the ‘same’ halos or galaxies at each redshift. Ideally we would like to be tracing the halo

mass along the merger trees of the same halos. Using our fitted SHMR, we can retrieve the stellar masses of halos along their merger histories from a dark-matter-only simulation. For this analysis, we retrieved the publicly available data from the dark-matter-only TNG300-1-Dark simulation (Pillepich et al. 2018). Starting from

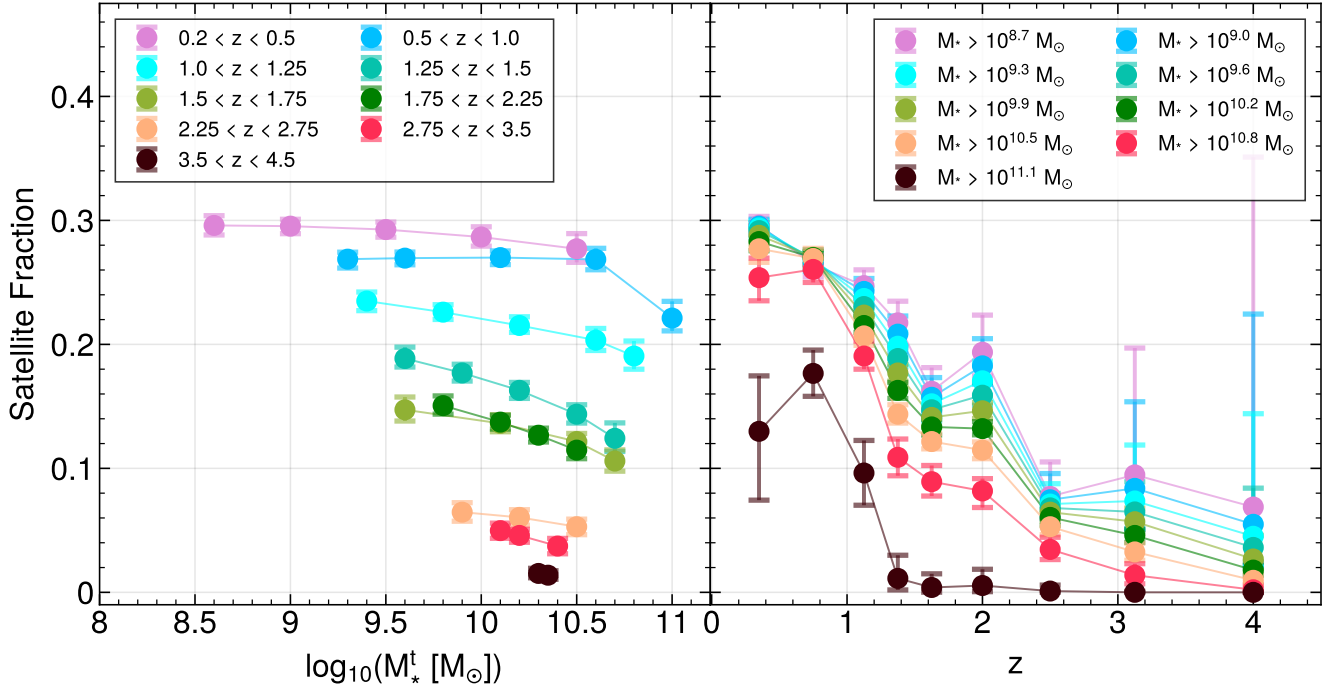


Figure 12. **Left:** Satellite fractions within each z -bin (as indicated in the legend) as a function of the stellar mass threshold, M_*^t of the sub-samples. **Right:** Satellite fractions of increasing stellar mass thresholds (as shown in the legend) as a function of redshift.

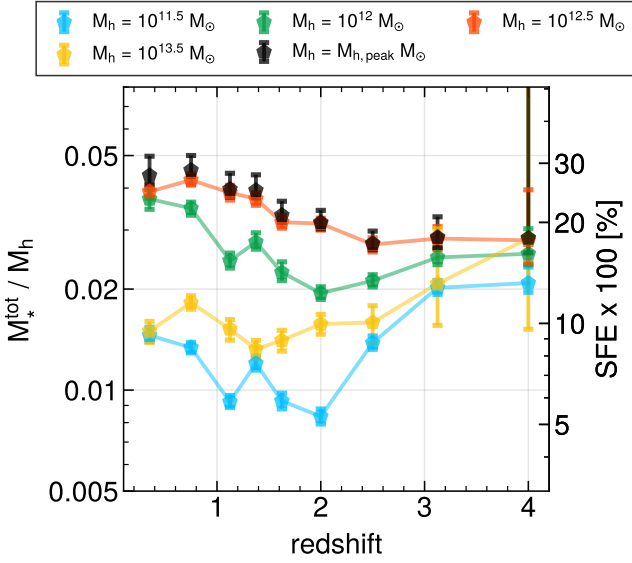


Figure 13. Redshift evolution of the total stellar mass-to-halo mass ratio, M_*^{tot}/M_h in halos of fixed mass. Different halo masses are indicated in the legend, and the SFE ($= (M_*^{\text{mean cen}}/M_h)/f_b$) in percentage is shown on the right y-axis.

$z \sim 0.2$ (snapshot number 84), the lowest redshift in our galaxy sample, we trace the sub-halo mass history along the main progenitor branch for the 2000 most massive halos. This results in final halo masses at $z \sim 0.2$ rang-

ing from $\sim 10^{12} M_\odot$ to $\sim 10^{16} M_\odot$ and their halo mass histories.

We divide the final halo masses in bins of 0.2 dex and within each bin, trace the mean of the halo mass histories. We convert these mean halo mass histories into M_*^{tot}/M_h histories using the M_*^{tot}/M_h at fixed halo masses shown in Figure 10. By calculating M_*^{tot}/M_h for each mean progenitor halo mass along the merger trees at medians of our z -bins, we trace the evolution of M_*^{tot}/M_h as the halo masses grow along the merger trees. The resulting M_*^{tot}/M_h along the merger trees are shown in the left panel of Figure 14. Similarly, we convert the $M_*^{\text{mean cen}}/M_h$ at fixed halo masses shown in Figure 7 into $M_*^{\text{mean cen}}/M_h$ along the merger trees and show the results in the right panel of Figure 14. In Figure 14, we indicate the mean halo masses with the sizes of the circles on the legend at the top. The final mean log halo mass, $\log_{10}(M_h [M_\odot])$ and the mean central galaxy stellar masses, $\log_{10}(<M_{* \text{cen}}> [M_\odot])$ at $z = 0.35$ (median of the lowest z -bin) are highlighted in different shades of red, as shown in the legend at the bottom, to guide the eye to trace their evolution.

Perhaps the most visually striking aspect of Figure 14 is the change in the hierarchy of SFE in halos with redshift. The highest mass halos have the highest SFE at $z \gtrsim 3$ and the order gets completely flipped by $z = 0.35$, where the lowest mass halos have the highest SFE. For instance, the highest average mass of halos ($M_h = 10^{13.8} M_\odot$) at $z = 0.35$ shown in the darkest shade of red, accumulates most of its stellar mass early

on at $z \gtrsim 3$, both in terms of the total stellar mass and that of only centrals, with SFE reaching $\sim 18\%$ and $\sim 12\%$, respectively. Below $z \sim 3$, this halo is found to be continually declining in SFE, getting completely quenched by $z = 0.35$.

This is in stark contrast to the lowest mean halo mass ($M_h = 10^{12.27} M_\odot$) considered at $z = 0.35$ which started building its stellar content much more recently at $z \lesssim 2$, with its SFE peaking ($\sim 28\%$ for the total stellar mass buildup in the left panel) only at $z \sim 0.35$. This is a clear sign of *downsizing* (Cowie et al. 1996) manifesting in the decline of the halo mass scale over time at which the SFE peaks - the highest mass halos assemble their stellar mass first followed by lesser and lesser massive halos.

Comparing the evolution of $M_*^{\text{mean cen}}/M_h$ (right panel) with M_*^{tot}/M_h (left panel), the increasing contribution of satellites with decreasing redshift is apparent and unsurprising as demonstrated by the overall increase in satellite fraction toward low redshift as seen in Figure 12. It also shows how the stellar mass growth of the most massive halos at low redshift is being driven almost entirely by satellite galaxies, with the opposite true of the lowest mass halos.

6. DISCUSSION

The evolution of SHMR has imprints of various physical processes integrated over halos' lifetimes such as cold gas flows towards the centers of halos giving rise to star formation, stellar/dark matter halo mass growth due to mergers, and on the flip side, the feedback effects that heat up or eject the gas out of galaxies quenching star formation. In light of our SHMR results in §5, here we try to build an intuition of the galaxy-halo connection and in turn its connection to galaxy formation.

6.1. The most star-forming halo mass - M_h^{peak}

We shall first look at the redshift evolution of the halo mass with peak SFE, M_h^{peak} as shown in Figure 8 (black line). This peak mass where the central galaxies peak in SFE equally applies to the total SHMR where the peak is dominated by the centrals.

6.1.1. Downsizing in M_h^{peak}

Interestingly, M_h^{peak} drops by 0.11 dex from $z \sim 1.4$ to $z \sim 0.35$, but remains consistent with no evolution beyond $z = 1.5$, as described in §5.4. Previous M_h^{peak} results in the literature (shown in Figure 8) had seen *downsizing* trends unanimously stronger than our ours (~ 0.26 dex as opposed to 0.11 dex in our case) at $z < 1.5$ and much stronger than ours in some studies like Shuntov et al. (2022) at $z > 1.5$. However, since these earlier results had been heavily based on a single field of COSMOS, it was not clear if the *downsizing* trends in M_h^{peak} were commonplace in the Universe. The use of two large fields in our work (UDS in conjunction with

COSMOS) greatly mitigated the effect of cosmic variance on M_h^{peak} evolution, and in doing so we found a much weaker *downsizing* signal throughout the redshifts probed.

Even though more widely separated and large fields are needed to constrain the M_h^{peak} out high redshift with better confidence, its *downsizing* trend might not be as strong or as universal as deduced from the COSMOS-based data. Peak integrated star formation occurs in a narrow channel of $M_h^{\text{peak}} \sim 10^{12.2} M_\odot - 10^{12.4} M_\odot$ out to $z = 4.5$, indicating tight coupling between halo mass assembly and galaxy stellar mass assembly, and that quenching strongly depends on halo mass. This is also supported by the small scatter in stellar mass at a fixed halo mass, $\sigma_{\log M_*}$ (~ 0.25 dex), again out to $z = 4.5$.

6.1.2. Implications on the strength of AGN feedback

The M_h^{peak} observed at any redshift results from the star formation history that preceded in a way to result in the most stellar mass per halo mass (M_*/M_h). Therefore, however minimal, the change in the M_h^{peak} holds clues to the strength of star formation regulating AGN feedback (Silk & Rees 1998; Benson et al. 2003) especially at the high-mass end. AGN feedback supposedly acts on the high mass halos ($\gtrsim 10^{12} M_\odot$) at least in the redshift range considered in this study. There are two broad classes of AGNs in the literature: i- '*jet-mode*' AGN: they expel their energy primarily through mechanical jets as they are radiatively inefficient, have low optical/ultraviolet (UV)/X-ray luminosities and low accretion rates with a thick toroidal disk. They generally host more massive black holes and are found more in redder, more massive quiescent galaxies and richer environments; ii- '*radiative-mode*' AGN: they are quite the opposite as their radiatively efficient thin disks allow them to expel their energy primarily through radiation instead of jets and are therefore much more luminous in optical/ultraviolet (UV)/X-ray wavelengths (Cielo et al. 2018; Heckman & Best 2014).

There is accumulating observational evidence that '*jet-mode*' AGN is responsible for much of the quenching in massive galaxies. For instance, Kondapally et al. (2023) analyzed a sample of ~ 1000 radio-excess AGNs within $0.5 < z < 2.5$ from the radio catalogs of LoTSS Deep Fields DR1 (Sabater et al. 2021; Tasse et al. 2021) and found that low-excitation (jet-mode) AGNs dominate the feedback across the full redshift range considered. On the contrary, '*radiative-mode*' AGNs are actually found to coexist with high levels of star formation. Florez et al. (2020) compared a sample of X-ray luminous AGNs with the galaxies that did not host an X-ray luminous AGN within $0.5 < z < 3$. They found X-ray luminous AGNs to be hosting much higher (by a factor of $\sim 3-10$) star-formation rates across the full range of redshifts and stellar mass considered. Florez et al.

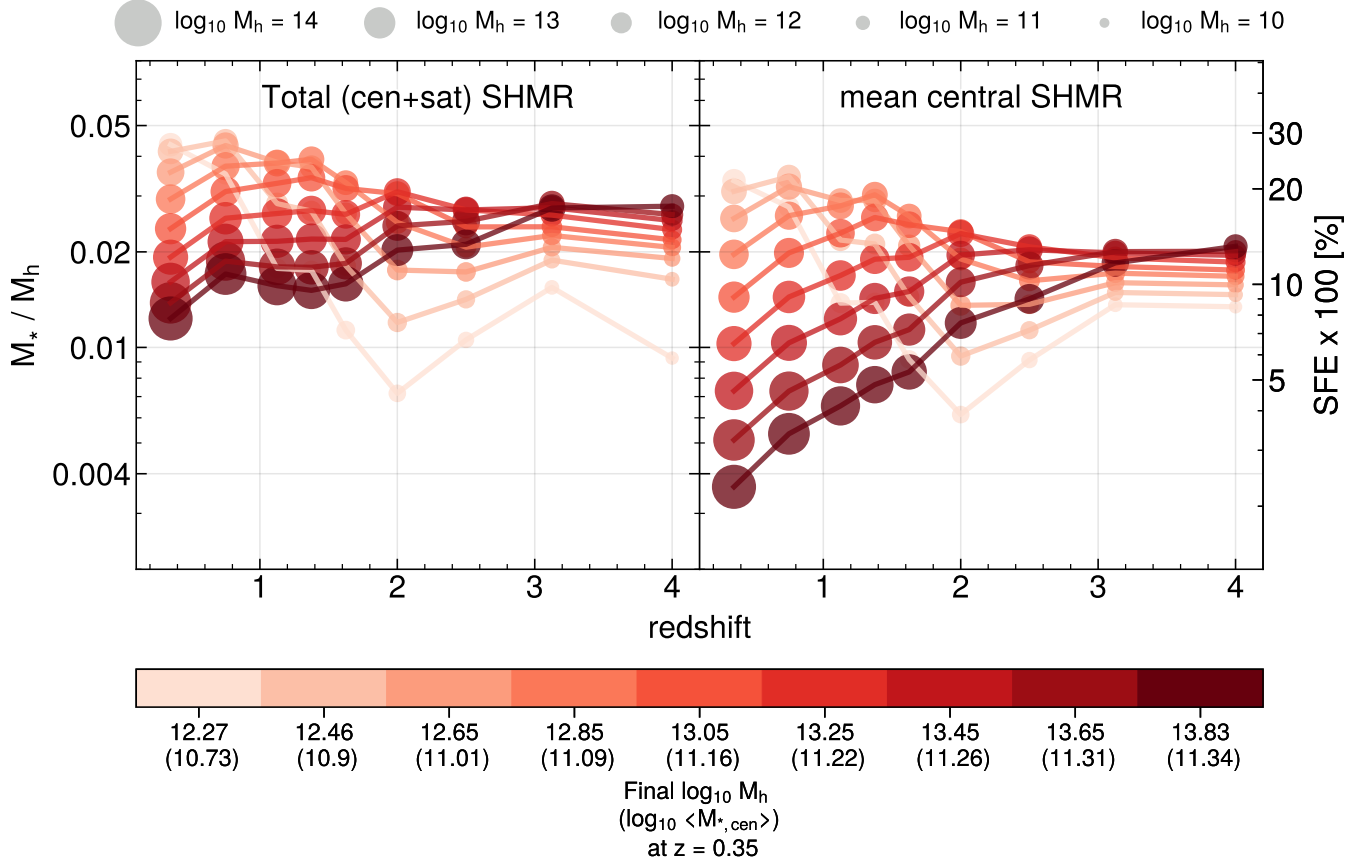


Figure 14. Left: Evolution of the total (centrals+satellites) stellar-halo mass ratio along the main progenitor branches (most massive branch) of $z = 0.35$ (median of the lowest z -bin in our analysis) dark matter halos in the TNG300-Dark-1 simulation (Pillepich et al. 2018). The total stellar mass in a given TNG300-Dark-1 halo mass (average in a 0.2 dex bin), depicted by the sizes of the red circles, is calculated using the fitted HOD model parameters at each redshift as described in §5.5. The shading of the circles and the lines connecting them reflect the final halo mass at $z = 0.35$ (as shown in the legend), where lighter shades of red depict lower final halo masses. **Right:** Evolution of the mean central stellar-halo mass ratio along the main progenitor branches of $z = 0.35$ dark matter halos in the TNG300-Dark-1 simulation as in the left panel. Again, this is evaluated at the best fit HOD parameters. As in the left panel, the colors of the circles represent the final halo masses (at $z = 0.35$), and their sizes capture the current halo masses.

(2021) find these results to be in general agreement with the simulations SAG (Cora et al. 2018) and IllustriTNG (Pillepich et al. 2018; Weinberger et al. 2017), while they see the opposite in their comparison to SIMBA (Davé et al. 2019). i.e. in SIMBA, high X-ray luminous AGNs are in fact found to have much lower levels of star formation and many are even quenched.

Therefore, for the following, we assume that it is the ‘jet-mode’ AGN feedback which is the dominant suppressor of star formation in massive galaxies and simply call it AGN feedback. Moving from high redshift to low redshift, if the AGN feedback had been weaker recently, higher mass halos become the most efficient in star formation, shifting M_h^{peak} toward higher masses. On the other hand, stronger AGN feedback in the recent past

of the observed redshift manifests in a lower M_h^{peak} at the observed redshift than otherwise.

Given the decrease in M_h^{peak} with time, albeit minimal, at least in our case, it is likely that the AGN feedback progresses by quenching the massive galaxies in decreasing order of stellar mass. This is also supported by the hierarchy of quenching as seen in Figure 14, where the most massive galaxies quench first followed by lesser and lesser massive galaxies. By $z \sim 1$, most of the massive galaxies in massive halos have quenched, whereas the lower mass halos are now peaking in SFE, thereby shifting the M_h^{peak} to its lowest value at $z \sim 0.35$.

6.2. Stellar-Halo mass growth

Figure 14 beautifully captures the *downsizing* trend in stellar-halo mass growth, i.e. they grow in decreasing order of mass. Group and cluster scales halos ($M_h \gtrsim$

$10^{13.5}$) at $z \sim 0.3$ hosting quenched galaxy population accumulated the bulk of the stellar mass early on, at $z \gtrsim 2$. Below $z \lesssim 2$, they are found with residual levels of star formation. On the other hand, the less massive halos ($M_h \lesssim 10^{12.7} M_\odot$) at $z \sim 0.3$ only started to build up their stellar mass at $z \lesssim 2$, reaching peak levels of star formation at $z \sim 0.3$. Now, we will examine the stellar-halo mass growth in these two regimes more closely.

6.2.1. Low mass regime

Throughout the redshift range considered in this study ($0.2 < z < 4.5$), on the lower side of the peak stellar-halo mass ratio (either of the M_h^{peak} or the peak in M_*^{tot}/M_h), stellar mass increases with increasing halo mass. As time passes, halos are expected to grow via merging with much smaller halos with lower stellar mass (Leauthaud et al. 2012; Legrand et al. 2019). Therefore, with an increase in halo mass, there will be a mild increase in stellar mass, but the M_*^{tot}/M_h should decline. Mergers alone cannot explain the steep rise in M_*^{tot}/M_h at $z \lesssim 2$; secular ‘in-situ’ star formation has to be invoked. At $z \gtrsim 2$, the low mass slope becomes shallower indicating lower levels of ‘in-situ’ star formation which is not surprising as star-forming efficiencies of low mass halos only pick up at $z \lesssim 2$, as seen through Figure 14.

6.2.2. High mass regime

As visible in Figure 10, the central galaxies dominate stellar mass within halos below the peak at $M_h \sim 10^{12} M_\odot$. Beyond this mass, in group-scale halos, the central contribution starts to decline and is taken over by the satellites. At first glance, this might indicate that the central galaxies suffer from a decline in SFE because the star-forming ability of the massive halos ($M_h \gtrsim 10^{12} M_\odot$) now gets distributed between centrals and satellites. However, upon close inspection, this does not seem to be the case, at least at $z \lesssim 1.5$. In the ‘satellite dominated’ regime (beyond $M_h \sim 10^{12} M_\odot$), even if all the stellar mass in satellites is somehow transferred to centrals, i.e. the solid M_*^{tot}/M_h curve becomes the $M_{*, cen}/M_h$ curve, the peak SFE remains at $M_h \sim 10^{12} M_\odot$, i.e. there is no second peak on the high mass end. This means that centrals in group-scale halos do not exceed the SFE obtained at $M_h \sim 10^{12} M_\odot$, *not* because the satellites take away their share of SFE, but rather that beyond $M_h \sim 10^{12} M_\odot$, there is a global decline in SFE of halos, again at least out to $z \sim 1.5$. Whatever quenching mechanism is at play in group-scale halos impacts both the central and satellites. This is in general agreement with Leauthaud et al. (2012) and Shuntov et al. (2022).

Interestingly at $z > 1.5$, M_*^{tot}/M_h seems to rise again beyond $M_h \sim 10^{13} M_\odot$ but it is hard to ascertain if it indeed overtakes the peak M_*^{tot}/M_h ratio obtained at $M_h \sim 10^{12} M_\odot$. This is because the upper limit on the halo mass probed by our analysis does not extend to high enough halo masses disallowing us to confidently

conclude if M_*^{tot}/M_h indeed overtakes the peak of $M_h \sim 10^{12} M_\odot$. Even if we extrapolate our models beyond the maximum halo mass probed at each redshift, the highest physically possible halo mass also decreases with redshift, thus leaving a very faint possibility of M_*^{tot}/M_h having a second peak at higher halo masses $M_h \gtrsim 10^{13} M_\odot$.

At $z > 1.5$, regardless if there is a second peak in M_h or not, there is an upturn in M_*^{tot}/M_h beyond $M_h \sim 10^{13} M_\odot$ due to satellites. The presence of this upturn and the lack thereof at $z < 1.5$ possibly conveys an important message: At $z > 1.5$, satellite accretion onto the massive halos is more prevalent which is plausible as the Universe was indeed more merger-ridden back then (Governato et al. 1999; Wetzel et al. 2009; Stewart et al. 2009). However, at $z < 1.5$, many of these satellites might have merged onto central galaxies, hence the suppression in the satellite contribution to M_*^{tot}/M_h for high halo masses.

7. SUMMARY

We present a comprehensive analysis of the stellar-to-halo mass relationship (SHMR) of central and satellite galaxies since $z = 4.5$. To derive the SHMRs, we fit the halo occupation distributions (HOD) models using measurements of galaxy clustering and abundance in two large legacy UDS and COSMOS fields, covering a total effective area of $\sim 1.61 \text{ deg}^2$. This is the first time that two photometric datasets (FENIKS v1 (UDS; Zaidi et al. (2024)) and UVISTA DR3 ultra-deep stripes (COSMOS; Muzzin et al. (2013)) of such area coverage and depth have been homogeneously integrated to trace stellar mass assembly within halos.

We also introduce a novel HOD fitting framework that allows the high constraining power of low- z data, due to more than ~ 3 dex of dynamical range in stellar mass where we are complete, to communicate with high- z ($z \gtrsim 2.5$), where we are complete only for $\lesssim 1$ dex. Data in all z -bins are jointly fitted where HOD parameters between adjacent z -bins are connected via continuity (smoothing) priors. This is motivated by the simple physical fact that galaxy clustering and abundance measurements between adjacent z -bins evolve from one to another, instead of being independent of each other. Therefore, HOD parameters between neighboring z -bins should not see abrupt changes. This allowed dramatically reducing the uncertainties in SHMR at $z > 2.5$, giving a much clearer picture of SHMR evolution out to $z = 4.5$. Our findings are as follows:

- We show that the halo mass with peak integrated star-forming efficiency (SFE), M_h^{peak} evolves very little: it stays between $\sim 10^{12.2} M_\odot$ and $\sim 10^{12.4} M_\odot$. At $z < 1.5$, we observe weak *downsizing* by 0.11 dex as opposed to ~ 0.26 dex in the COSMOS-based studies (see §5.4). We attribute this difference to the presence of over-dense SMFs of COSMOS due to many reported over-dense structure (see §5.4.1). Beyond $z > 1.5$, we

see insignificant evolution in M_h^{peak} as opposed to steep *downsizing* found in other COSMOS-based studies like Shuntov et al. (2022), albeit with large error-bars.

- The total stellar mass locked up in halos less massive than $M_h \sim 10^{12} M_\odot$ is dominated by central galaxies, whereas satellites dominate the stellar mass budget beyond $M_h \sim 10^{13} M_\odot$ in group and cluster scale halos (see §5.5).

- The conditional stellar mass function (SMF) of central galaxies depends strongly on halo mass. It peaks at increasingly larger stellar masses for increasing halo masses, and tails off on either end. Satellites’ conditional SMFs, however, depend much more weakly on halo mass; satellites are equally scattered across $M_h = 10^{11.5} - 10^{13.5} M_\odot$ at $M_* \lesssim 10^{10} M_\odot$. Overall, the conditional satellite SMFs have a classic SMF shape with a power law at low masses, ‘knee’ at intermediate masses, beyond which it declines sharply (see §5.6).

- The fraction of mass in satellites, f_{sat} generally increases with decreasing redshift and stellar mass thresholds. f_{sat} never exceeds $\sim 30\%$ attained within the lowest z -bin and stellar mass threshold considered (see §5.7).

- We show in Figure 14 the evolution in SFE of halos, for the first time, as they grow along their progenitor merger trees. Star formation occurs hierarchically: most

massive halos and galaxies observed within the lowest z -bin ($z \sim 0.35$) accumulate their stellar mass first followed by progressively lighter systems. This hierarchy applies to both central and satellite galaxies (see §5.9).

8. ACKNOWLEDGMENTS

KZ acknowledges the John F. Burlingame Graduate Fellowship in the Physics & Astronomy Department at Tufts University for support while conducting majority of this work. KZ and DM acknowledge support from the National Science Foundation under grant AST-2009442. Additionally, CP and JAD acknowledge support from the National Science Foundation under grant AST-2009632. K.G. acknowledges support from Australian Research Council Laureate Fellowship FL180100060.

The authors acknowledge the Tufts University High Performance Compute Cluster (<https://it.tufts.edu/high-performance-computing>) which was utilized for the research reported in this paper.

Software: Astropy (Astropy Collaboration et al. 2022), numpy (Harris et al. 2020), halomod (Murray et al. 2021), CORRFUNC (Sinha & Garrison 2020; Sinha & Garrison 2019), pycorr

APPENDIX

A. COMBINED STELLAR MASS FUNCTIONS OF UDS AND COSMOS

In Tables 3 - 11, we present the combined SMFs calculated using the FENIKS v1 (UDS) (Zaidi et al. 2024) and ultra-deep stripes of UVISTA DR3 (COSMOS) (Muzzin et al. 2013), the datasets utilized in this study.

B. EXAMPLE HOD POSTERiors FOR “SMOOTH-Z” VERSUS “DISCREET-Z” MODELS

We showcase the improvement in fitting due to the implementation of “smooth- z ” model over “discreet- z ” model, specially at high- z , through their corner plots showing HOD posteriors in Figures 15–18.

REFERENCES

- Ashby, M. L. N., Caputi, K. I., Cowley, W., et al. 2018, ApJS, 237, 39, doi: [10.3847/1538-4365/aad4fb](https://doi.org/10.3847/1538-4365/aad4fb)
- Astropy Collaboration, Price-Whelan, A. M., Lim, P. L., et al. 2022, ApJ, 935, 167, doi: [10.3847/1538-4357/ac7c74](https://doi.org/10.3847/1538-4357/ac7c74)
- Behroozi, P., Wechsler, R. H., Hearin, A. P., & Conroy, C. 2019, MNRAS, 488, 3143, doi: [10.1093/mnras/stz1182](https://doi.org/10.1093/mnras/stz1182)
- Behroozi, P. S., Conroy, C., & Wechsler, R. H. 2010, ApJ, 717, 379, doi: [10.1088/0004-637X/717/1/379](https://doi.org/10.1088/0004-637X/717/1/379)

Table 3. $0.2 < z < 0.5$

$\log_{10}(M_* [M_{\odot}])_{bin}$	N_{gal}	$\log_{10}(\Phi [\text{Mpc}^{-3} \text{dex}^{-1}])$
8.6 - 8.8	5130	$-1.5951^{+0.0392}_{-0.0392}$
8.8 - 9.0	4290	$-1.6728^{+0.0397}_{-0.0397}$
9.0 - 9.2	3207	$-1.7991^{+0.0403}_{-0.0403}$
9.2 - 9.4	2459	$-1.9145^{+0.0411}_{-0.0411}$
9.4 - 9.6	1982	$-2.0081^{+0.0419}_{-0.0419}$
9.6 - 9.8	1476	$-2.1362^{+0.043}_{-0.043}$
9.8 - 10.0	1305	$-2.1896^{+0.0442}_{-0.0442}$
10.0 - 10.2	1193	$-2.2286^{+0.0456}_{-0.0456}$
10.2 - 10.4	956	$-2.3248^{+0.0472}_{-0.0472}$
10.4 - 10.6	869	$-2.3662^{+0.0484}_{-0.0484}$
10.6 - 10.8	832	$-2.3851^{+0.0496}_{-0.0496}$
10.8 - 11.0	631	$-2.5052^{+0.054}_{-0.054}$
11.0 - 11.2	417	$-2.6851^{+0.06}_{-0.06}$
11.2 - 11.4	230	$-2.9435^{+0.0676}_{-0.0677}$
11.4 - 11.6	96	$-3.323^{+0.0804}_{-0.0805}$
11.6 - 11.8	16	$-4.1011^{+0.1389}_{-0.142}$
11.8 - 12.0	3	$-4.8281^{+0.3039}_{-0.3479}$

Table 4. $0.5 < z < 1.0$

$\log_{10}(M_* [M_{\odot}])_{bin}$	N_{gal}	$\log_{10}(\Phi [\text{Mpc}^{-3} \text{dex}^{-1}])$
9.3 - 9.5	10173	$-1.9732^{+0.0277}_{-0.0277}$
9.5 - 9.7	8434	$-2.0546^{+0.028}_{-0.028}$
9.7 - 9.9	6716	$-2.1535^{+0.0285}_{-0.0285}$
9.9 - 10.1	5351	$-2.2522^{+0.0294}_{-0.0294}$
10.1 - 10.3	4372	$-2.3399^{+0.0303}_{-0.0303}$
10.3 - 10.5	3805	$-2.4003^{+0.0313}_{-0.0313}$
10.5 - 10.7	3488	$-2.438^{+0.0324}_{-0.0324}$
10.7 - 10.9	3102	$-2.489^{+0.0342}_{-0.0342}$
10.9 - 11.1	2490	$-2.5844^{+0.0385}_{-0.0385}$
11.1 - 11.3	1616	$-2.7722^{+0.043}_{-0.043}$
11.3 - 11.5	684	$-3.1456^{+0.0488}_{-0.0488}$
11.5 - 11.7	237	$-3.6059^{+0.0578}_{-0.0578}$
11.7 - 11.9	35	$-4.4365^{+0.0956}_{-0.0965}$

Table 5. $1.0 < z < 1.25$

$\log_{10}(M_* [M_{\odot}]_{bin})$	N_{gal}	$\log_{10}(\Phi [\text{Mpc}^{-3} \text{ dex}^{-1}])$
9.4 - 9.6	5246	$-2.1343^{+0.0345}_{-0.0345}$
9.6 - 9.8	4531	$-2.1979^{+0.035}_{-0.035}$
9.8 - 10.0	3717	$-2.2839^{+0.036}_{-0.036}$
10.0 - 10.2	2753	$-2.4143^{+0.0374}_{-0.0374}$
10.2 - 10.4	2218	$-2.5082^{+0.039}_{-0.039}$
10.4 - 10.6	1765	$-2.6074^{+0.0412}_{-0.0412}$
10.6 - 10.8	1541	$-2.6663^{+0.0434}_{-0.0434}$
10.8 - 11.0	1326	$-2.7316^{+0.0493}_{-0.0493}$
11.0 - 11.2	953	$-2.875^{+0.0568}_{-0.0568}$
11.2 - 11.4	550	$-3.1138^{+0.0649}_{-0.0649}$
11.4 - 11.6	200	$-3.5531^{+0.0761}_{-0.0762}$
11.6 - 11.8	45	$-4.2009^{+0.1029}_{-0.1034}$
11.8 - 12.0	10	$-4.8541^{+0.1753}_{-0.1817}$

Table 6. $1.25 < z < 1.5$

$\log_{10}(M_* [M_{\odot}]_{bin})$	N_{gal}	$\log_{10}(\Phi [\text{Mpc}^{-3} \text{ dex}^{-1}])$
9.6 - 9.8	5318	$-2.1876^{+0.035}_{-0.035}$
9.8 - 10.0	4287	$-2.2812^{+0.0362}_{-0.0362}$
10.0 - 10.2	3530	$-2.3655^{+0.0375}_{-0.0375}$
10.2 - 10.4	2777	$-2.4697^{+0.0392}_{-0.0392}$
10.4 - 10.6	2160	$-2.5789^{+0.0419}_{-0.0419}$
10.6 - 10.8	1717	$-2.6785^{+0.0447}_{-0.0447}$
10.8 - 11.0	1333	$-2.7885^{+0.0516}_{-0.0516}$
11.0 - 11.2	918	$-2.9505^{+0.0602}_{-0.0602}$
11.2 - 11.4	468	$-3.2431^{+0.0697}_{-0.0697}$
11.4 - 11.6	164	$-3.6985^{+0.0826}_{-0.0826}$
11.6 - 11.8	31	$-4.422^{+0.118}_{-0.119}$
11.8 - 12.0	3	$-5.4362^{+0.3081}_{-0.3516}$

Table 7. $1.5 < z < 1.75$

$\log_{10}(M_* [M_{\odot}])_{bin}$	N_{gal}	$\log_{10}(\Phi [\text{Mpc}^{-3} \text{dex}^{-1}])$
9.6 - 9.8	4075	$-2.3388^{+0.0362}_{-0.0362}$
9.8 - 10.0	3554	$-2.3983^{+0.0374}_{-0.0374}$
10.0 - 10.2	2865	$-2.4918^{+0.0388}_{-0.0388}$
10.2 - 10.4	2279	$-2.5912^{+0.0408}_{-0.0408}$
10.4 - 10.6	1769	$-2.7012^{+0.0442}_{-0.0442}$
10.6 - 10.8	1307	$-2.8327^{+0.0477}_{-0.0477}$
10.8 - 11.0	933	$-2.9791^{+0.0558}_{-0.0559}$
11.0 - 11.2	600	$-3.1708^{+0.0659}_{-0.0659}$
11.2 - 11.4	287	$-3.4911^{+0.0774}_{-0.0774}$
11.4 - 11.6	90	$-3.9947^{+0.0951}_{-0.0952}$
11.6 - 11.8	21	$-4.6268^{+0.1381}_{-0.1398}$
11.8 - 12.0	2	$-5.6479^{+0.378}_{-0.4597}$

Table 8. $1.75 < z < 2.25$

$\log_{10}(M_* [M_{\odot}])_{bin}$	N_{gal}	$\log_{10}(\Phi [\text{Mpc}^{-3} \text{dex}^{-1}])$
9.8 - 10.0	5870	$-2.5075^{+0.0306}_{-0.0306}$
10.0 - 10.2	4695	$-2.6045^{+0.0317}_{-0.0317}$
10.2 - 10.4	3720	$-2.7056^{+0.0333}_{-0.0333}$
10.4 - 10.6	2821	$-2.8257^{+0.0366}_{-0.0366}$
10.6 - 10.8	1887	$-3.0003^{+0.04}_{-0.04}$
10.8 - 11.0	1248	$-3.1799^{+0.0472}_{-0.0472}$
11.0 - 11.2	785	$-3.3812^{+0.056}_{-0.056}$
11.2 - 11.4	396	$-3.6784^{+0.0658}_{-0.0658}$
11.4 - 11.6	164	$-4.0613^{+0.0782}_{-0.0783}$
11.6 - 11.8	30	$-4.799^{+0.1158}_{-0.1168}$
11.8 - 12.0	2	$-5.9751^{+0.3743}_{-0.4567}$

Behroozi, P. S., Wechsler, R. H., & Conroy, C. 2013, ApJ, 770, 57, doi: [10.1088/0004-637X/770/1/57](https://doi.org/10.1088/0004-637X/770/1/57)

Benson, A. J., Bower, R. G., Frenk, C. S., et al. 2003, ApJ, 599, 38, doi: [10.1086/379160](https://doi.org/10.1086/379160)

Berlind, A. A., Weinberg, D. H., Benson, A. J., et al. 2003, ApJ, 593, 1, doi: [10.1086/376517](https://doi.org/10.1086/376517)

Blake, C., Collister, A., & Lahav, O. 2008, MNRAS, 385, 1257, doi: [10.1111/j.1365-2966.2007.11925.x](https://doi.org/10.1111/j.1365-2966.2007.11925.x)

Bower, R. G., Benson, A. J., Malbon, R., et al. 2006, MNRAS, 370, 645, doi: [10.1111/j.1365-2966.2006.10519.x](https://doi.org/10.1111/j.1365-2966.2006.10519.x)

Brammer, G. B., van Dokkum, P. G., & Coppi, P. 2008, ApJ, 686, 1503, doi: [10.1086/591786](https://doi.org/10.1086/591786)

Calzetti, D., Armus, L., Bohlin, R. C., et al. 2000, ApJ, 533, 682, doi: [10.1086/308692](https://doi.org/10.1086/308692)

Chabrier, G. 2003, PASP, 115, 763, doi: [10.1086/376392](https://doi.org/10.1086/376392)

Cielo, S., Bieri, R., Volonteri, M., Wagner, A. Y., & Dubois, Y. 2018, MNRAS, 477, 1336, doi: [10.1093/mnras/sty708](https://doi.org/10.1093/mnras/sty708)

Cole, S., Lacey, C. G., Baugh, C. M., & Frenk, C. S. 2000, MNRAS, 319, 168, doi: [10.1046/j.1365-8711.2000.03879.x](https://doi.org/10.1046/j.1365-8711.2000.03879.x)

Conroy, C., & Wechsler, R. H. 2009, ApJ, 696, 620, doi: [10.1088/0004-637X/696/1/620](https://doi.org/10.1088/0004-637X/696/1/620)

Cora, S. A., Vega-Martínez, C. A., Hough, T., et al. 2018, MNRAS, 479, 2, doi: [10.1093/mnras/sty1131](https://doi.org/10.1093/mnras/sty1131)

Coupon, J., Kilbinger, M., McCracken, H. J., et al. 2012, A&A, 542, A5, doi: [10.1051/0004-6361/201117625](https://doi.org/10.1051/0004-6361/201117625)

Table 9. $2.25 < z < 2.75$

$\log_{10}(M_* [M_{\odot}])_{bin}$	N_{gal}	$\log_{10}(\Phi [\text{Mpc}^{-3} \text{dex}^{-1}])$
9.9 - 10.1	4968	$-2.5889^{+0.036}_{-0.036}$
10.1 - 10.3	3953	$-2.6882^{+0.0372}_{-0.0372}$
10.3 - 10.5	2749	$-2.8459^{+0.0412}_{-0.0412}$
10.5 - 10.7	1739	$-3.0448^{+0.0462}_{-0.0462}$
10.7 - 10.9	993	$-3.2881^{+0.053}_{-0.053}$
10.9 - 11.1	511	$-3.5767^{+0.0646}_{-0.0646}$
11.1 - 11.3	271	$-3.8521^{+0.077}_{-0.077}$
11.3 - 11.5	69	$-4.4462^{+0.0991}_{-0.0993}$
11.5 - 11.7	29	$-4.8227^{+0.1272}_{-0.1282}$
11.7 - 11.9	4	$-5.683^{+0.2727}_{-0.3}$

Table 10. $2.75 < z < 3.5$

$\log_{10}(M_* [M_{\odot}])_{bin}$	N_{gal}	$\log_{10}(\Phi [\text{Mpc}^{-3} \text{dex}^{-1}])$
10.1 - 10.3	5261	$-2.7287^{+0.0388}_{-0.0388}$
10.3 - 10.5	3246	$-2.9384^{+0.0437}_{-0.0437}$
10.5 - 10.7	1521	$-3.2676^{+0.0503}_{-0.0503}$
10.7 - 10.9	631	$-3.6497^{+0.059}_{-0.059}$
10.9 - 11.1	249	$-4.0536^{+0.0733}_{-0.0733}$
11.1 - 11.3	118	$-4.3779^{+0.0892}_{-0.0893}$
11.3 - 11.5	39	$-4.8587^{+0.1169}_{-0.1175}$
11.5 - 11.7	10	$-5.4498^{+0.1844}_{-0.1905}$
11.7 - 11.9	7	$-5.6047^{+0.218}_{-0.2288}$

Table 11. $3.5 < z < 4.5$

$\log_{10}(M_* [M_{\odot}])_{bin}$	N_{gal}	$\log_{10}(\Phi [\text{Mpc}^{-3} \text{dex}^{-1}])$
10.3 - 10.5	1795	$-3.2876^{+0.0548}_{-0.0548}$
10.5 - 10.7	753	$-3.6649^{+0.0647}_{-0.0647}$
10.7 - 10.9	212	$-4.2153^{+0.079}_{-0.079}$
10.9 - 11.1	86	$-4.6072^{+0.0994}_{-0.0995}$
11.1 - 11.3	21	$-5.2195^{+0.1439}_{-0.1456}$
11.3 - 11.5	8	$-5.6386^{+0.2076}_{-0.2162}$

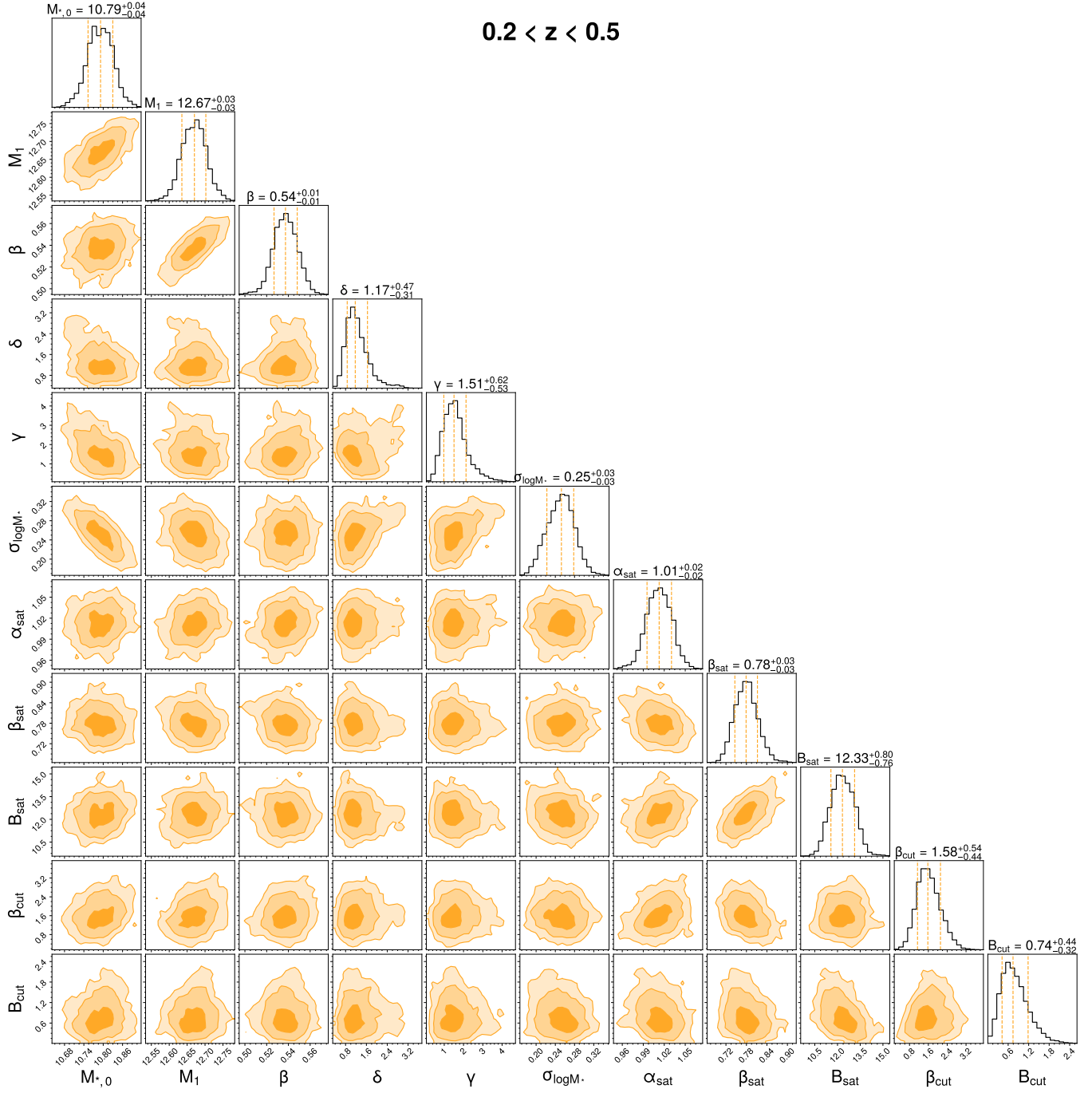


Figure 15. “smooth- z ” model corner plot showing HOD posteriors at $0.2 < z < 0.5$, where we jointly fitted data in all the z -bins out to $z = 4.5$ as described in §4.8). The median values and the 1σ uncertainty are shown on top of the 1-D projected marginalized distributions along the diagonal of the figure. The 2-D projected marginalized distributions of pairs of parameters are shown with contours with lightening shades of yellow going from 1σ (darkest) to 2σ to 3σ (lightest).

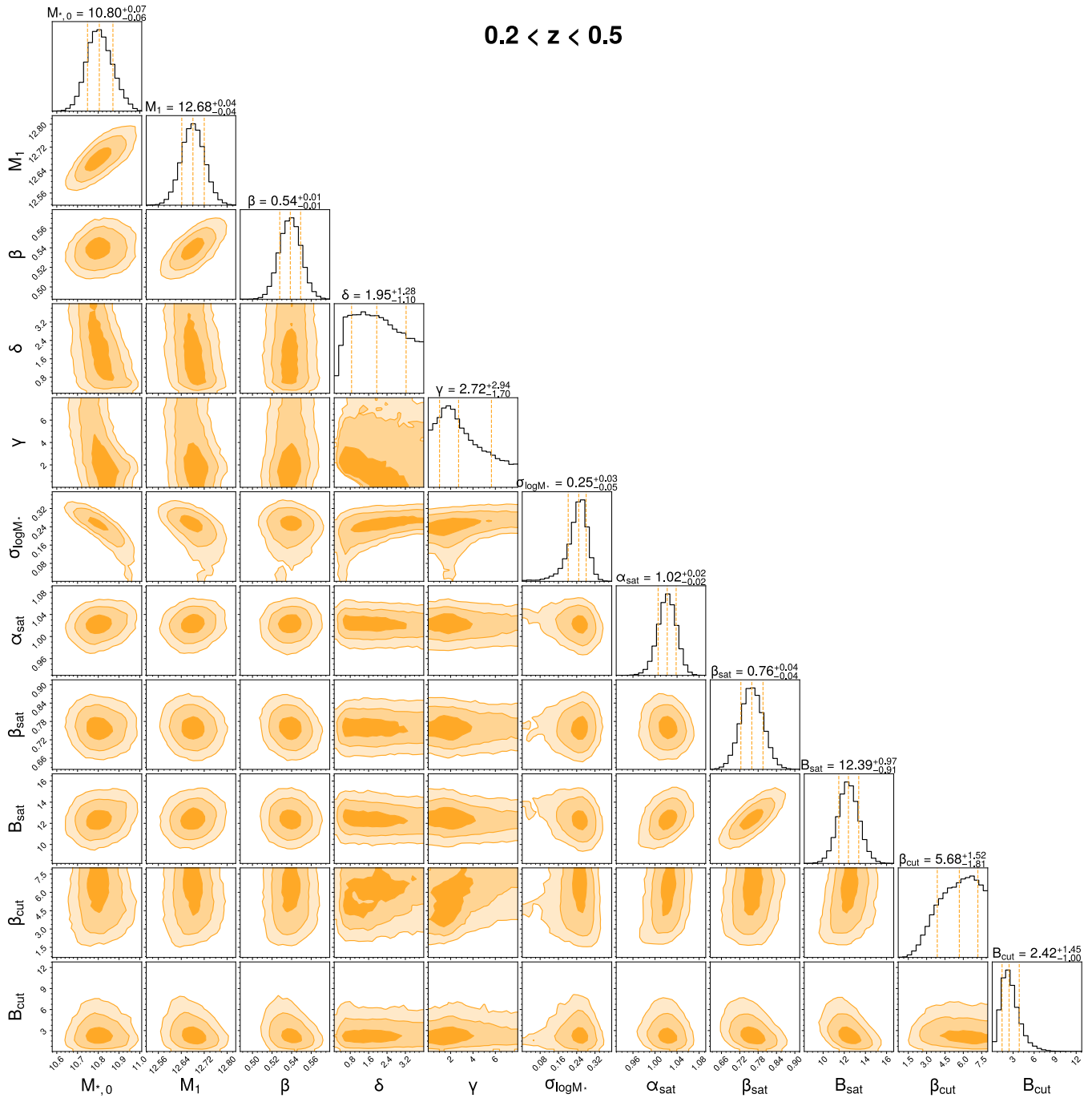


Figure 16. “discreet- z ” model corner plot showing HOD posteriors at $0.2 < z < 0.5$ plotted as in Figure 15.

Coupon, J., Arnouts, S., van Waerbeke, L., et al. 2015, MNRAS, 449, 1352, doi: [10.1093/mnras/stv276](https://doi.org/10.1093/mnras/stv276)

Cowie, L. L., Songaila, A., Hu, E. M., & Cohen, J. G. 1996, AJ, 112, 839, doi: [10.1086/118058](https://doi.org/10.1086/118058)

Cowley, W. I., Caputi, K. I., Deshmukh, S., et al. 2018, ApJ, 853, 69, doi: [10.3847/1538-4357/aaa41d](https://doi.org/10.3847/1538-4357/aaa41d)

Croton, D. J., Springel, V., White, S. D. M., et al. 2006, MNRAS, 365, 11, doi: [10.1111/j.1365-2966.2005.09675.x](https://doi.org/10.1111/j.1365-2966.2005.09675.x)

Darvish, B., Sobral, D., Mobasher, B., et al. 2014, ApJ, 796, 51, doi: [10.1088/0004-637X/796/1/51](https://doi.org/10.1088/0004-637X/796/1/51)

Davé, R., Anglés-Alcázar, D., Narayanan, D., et al. 2019, MNRAS, 486, 2827, doi: [10.1093/mnras/stz937](https://doi.org/10.1093/mnras/stz937)

Davidzon, I., Ilbert, O., Laigle, C., et al. 2017, A&A, 605, A70, doi: [10.1051/0004-6361/201730419](https://doi.org/10.1051/0004-6361/201730419)

De Lucia, G., & Blaizot, J. 2007, MNRAS, 375, 2, doi: [10.1111/j.1365-2966.2006.11287.x](https://doi.org/10.1111/j.1365-2966.2006.11287.x)

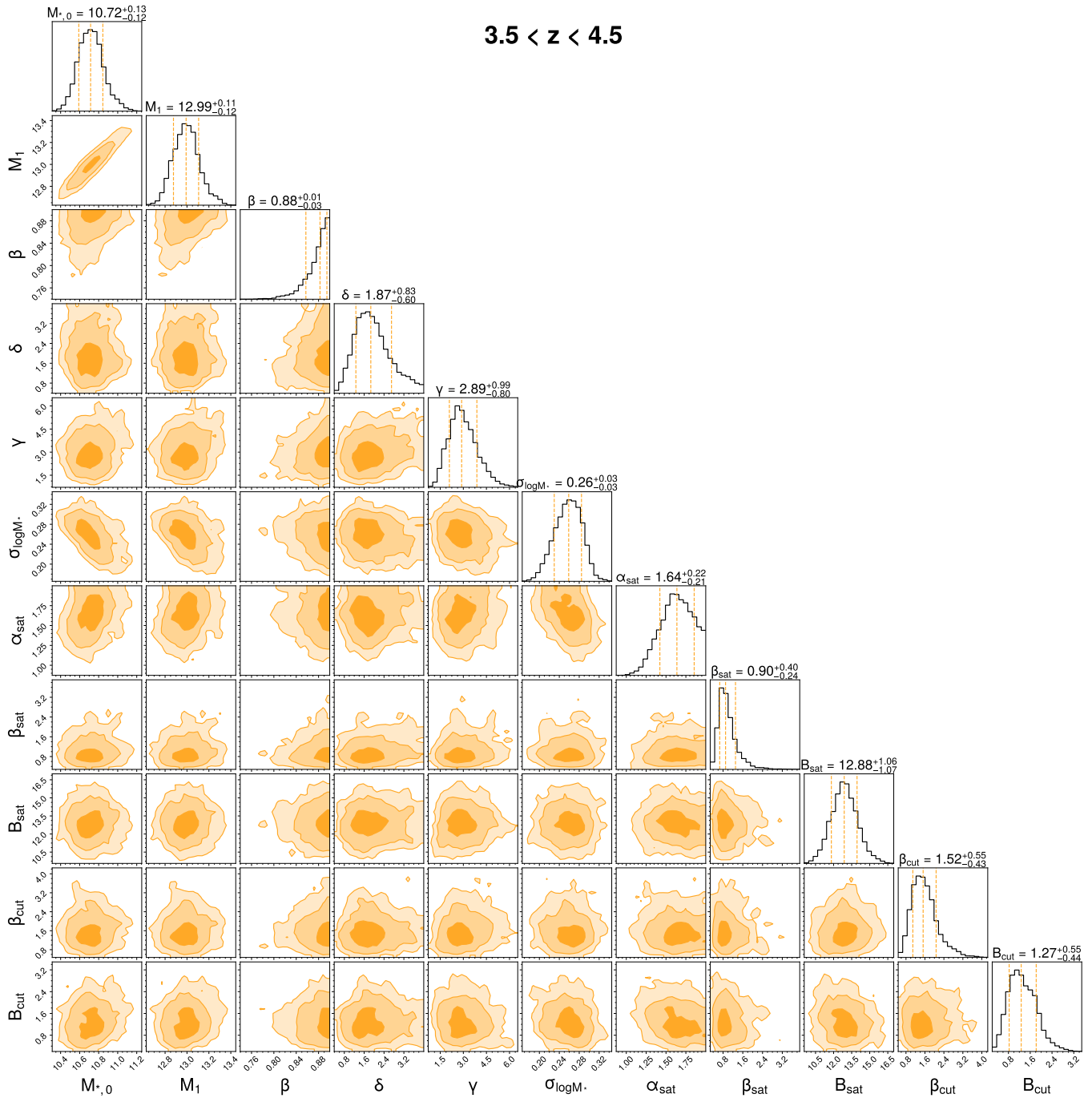


Figure 17. “smooth- z ” model corner plot showing HOD posteriors at $3.5 < z < 4.5$ plotted as in Figure 15.

Fall, S. M., & Efstathiou, G. 1980, MNRAS, 193, 189,
doi: [10.1093/mnras/193.2.189](https://doi.org/10.1093/mnras/193.2.189)

Florez, J., Jogee, S., Sherman, S., et al. 2020, MNRAS, 497,
3273, doi: [10.1093/mnras/staa2200](https://doi.org/10.1093/mnras/staa2200)

Florez, J., Jogee, S., Guo, Y., et al. 2021, MNRAS, 508,
762, doi: [10.1093/mnras/stab2593](https://doi.org/10.1093/mnras/stab2593)

Foreman-Mackey, D., Hogg, D. W., Lang, D., & Goodman,
J. 2013, PASP, 125, 306, doi: [10.1086/670067](https://doi.org/10.1086/670067)

Gehrels, N. 1986, ApJ, 303, 336, doi: [10.1086/164079](https://doi.org/10.1086/164079)

Goodman, J., & Weare, J. 2010, Communications in
Applied Mathematics and Computational Science, 5, 65,
doi: [10.2140/camcos.2010.5.65](https://doi.org/10.2140/camcos.2010.5.65)

Governato, F., Gardner, J. P., Stadel, J., Quinn, T., &
Lake, G. 1999, AJ, 117, 1651, doi: [10.1086/300805](https://doi.org/10.1086/300805)

Groth, E. J., & Peebles, P. J. E. 1977, ApJ, 217, 385,
doi: [10.1086/155588](https://doi.org/10.1086/155588)

Guo, Q., White, S., Boylan-Kolchin, M., et al. 2011,
MNRAS, 413, 101, doi: [10.1111/j.1365-2966.2010.18114.x](https://doi.org/10.1111/j.1365-2966.2010.18114.x)

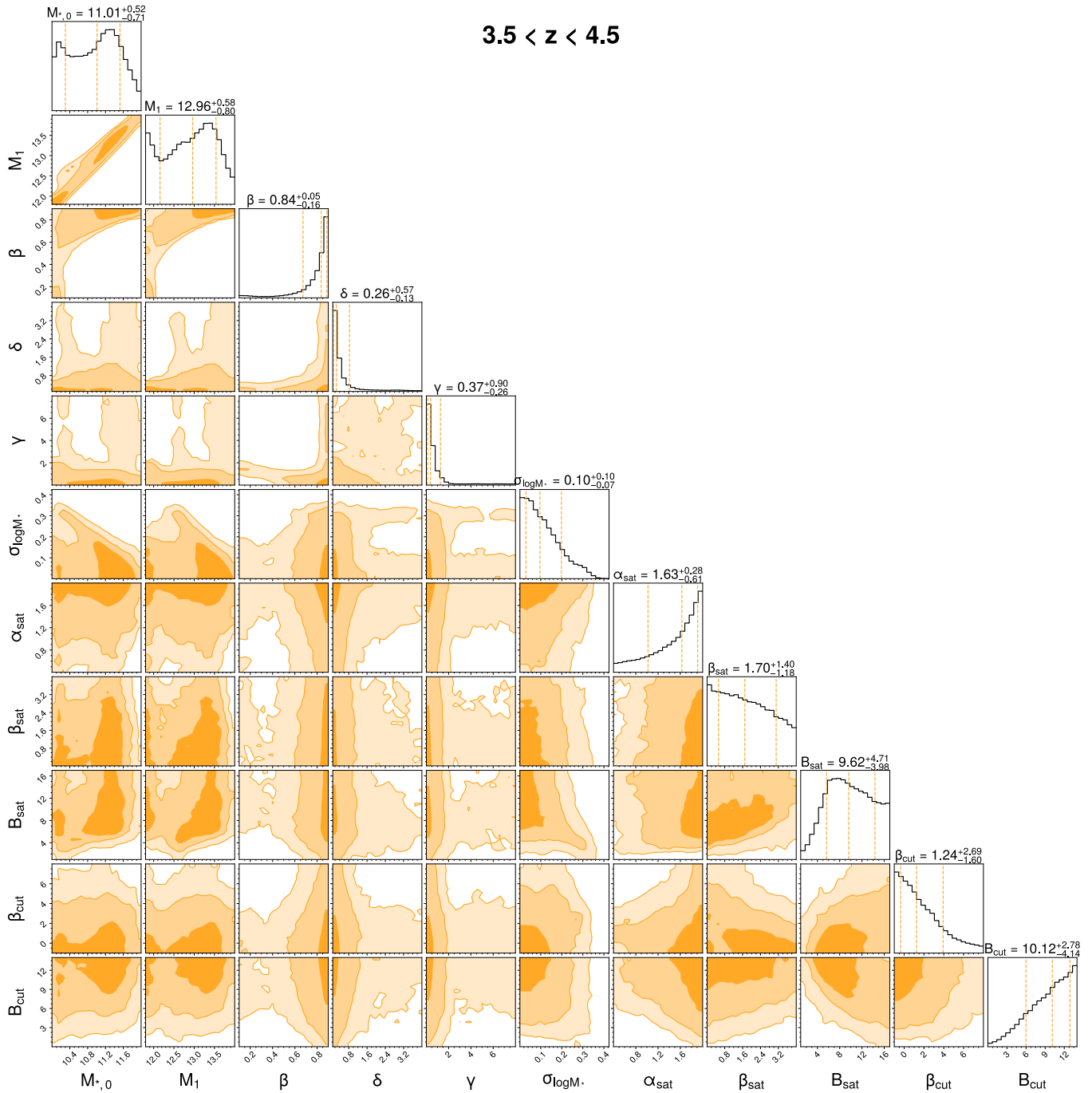


Figure 18. “discreet- z ” model corner plot showing HOD posteriors at $3.5 < z < 4.5$ plotted as in Figure 15.

Harris, C. R., Millman, K. J., van der Walt, S. J., et al. 2020, *Nature*, 585, 357, doi: [10.1038/s41586-020-2649-2](https://doi.org/10.1038/s41586-020-2649-2)

Heckman, T. M., & Best, P. N. 2014, *ARA&A*, 52, 589, doi: [10.1146/annurev-astro-081913-035722](https://doi.org/10.1146/annurev-astro-081913-035722)

Henriques, B. M. B., White, S. D. M., Thomas, P. A., et al. 2015, *MNRAS*, 451, 2663, doi: [10.1093/mnras/stv705](https://doi.org/10.1093/mnras/stv705)

Henriques, B. M. B., Yates, R. M., Fu, J., et al. 2020, *MNRAS*, 491, 5795, doi: [10.1093/mnras/stz3233](https://doi.org/10.1093/mnras/stz3233)

Hopkins, P. F., Quataert, E., & Murray, N. 2012, *MNRAS*, 421, 3522, doi: [10.1111/j.1365-2966.2012.20593.x](https://doi.org/10.1111/j.1365-2966.2012.20593.x)

Hopkins, P. F., Wetzel, A., Wheeler, C., et al. 2023, *MNRAS*, 519, 3154, doi: [10.1093/mnras/stac3489](https://doi.org/10.1093/mnras/stac3489)

Infante, L. 1994, *A&A*, 282, 353

Ishikawa, S., Kashikawa, N., Toshikawa, J., et al. 2017, *ApJ*, 841, 8, doi: [10.3847/1538-4357/aa6d64](https://doi.org/10.3847/1538-4357/aa6d64)

Iyer, K., & Gawiser, E. 2017, *ApJ*, 838, 127, doi: [10.3847/1538-4357/aa63f0](https://doi.org/10.3847/1538-4357/aa63f0)

- Iyer, K. G., Gawiser, E., Faber, S. M., et al. 2019, *ApJ*, 879, 116, doi: [10.3847/1538-4357/ab2052](https://doi.org/10.3847/1538-4357/ab2052)
- Juneau, S., Glazebrook, K., Crampton, D., et al. 2005, *ApJL*, 619, L135, doi: [10.1086/427937](https://doi.org/10.1086/427937)
- Kondapally, R., Best, P. N., Raouf, M., et al. 2023, *MNRAS*, 523, 5292, doi: [10.1093/mnras/stad1813](https://doi.org/10.1093/mnras/stad1813)
- Kravtsov, A. V., Berlind, A. A., Wechsler, R. H., et al. 2004, *ApJ*, 609, 35, doi: [10.1086/420959](https://doi.org/10.1086/420959)
- Kriek, M., van Dokkum, P. G., Labbé, I., et al. 2009, *ApJ*, 700, 221, doi: [10.1088/0004-637X/700/1/221](https://doi.org/10.1088/0004-637X/700/1/221)
- Landy, S. D., & Szalay, A. S. 1993, *ApJ*, 412, 64, doi: [10.1086/172900](https://doi.org/10.1086/172900)
- Leauthaud, A., Tinker, J., Behroozi, P. S., Busha, M. T., & Wechsler, R. H. 2011, *ApJ*, 738, 45, doi: [10.1088/0004-637X/738/1/45](https://doi.org/10.1088/0004-637X/738/1/45)
- Leauthaud, A., Tinker, J., Bundy, K., et al. 2012, *ApJ*, 744, 159, doi: [10.1088/0004-637X/744/2/159](https://doi.org/10.1088/0004-637X/744/2/159)
- Legrand, L., McCracken, H. J., Davidzon, I., et al. 2019, *MNRAS*, 486, 5468, doi: [10.1093/mnras/stz1198](https://doi.org/10.1093/mnras/stz1198)
- Limber, D. N. 1954, *ApJ*, 119, 655, doi: [10.1086/145870](https://doi.org/10.1086/145870)
- Mandelbaum, R., Seljak, U., Kauffmann, G., Hirata, C. M., & Brinkmann, J. 2006, *MNRAS*, 368, 715, doi: [10.1111/j.1365-2966.2006.10156.x](https://doi.org/10.1111/j.1365-2966.2006.10156.x)
- Marinoni, C., & Hudson, M. J. 2002, *ApJ*, 569, 101, doi: [10.1086/339319](https://doi.org/10.1086/339319)
- McCracken, H. J., Milvang-Jensen, B., Dunlop, J., et al. 2012, *A&A*, 544, A156, doi: [10.1051/0004-6361/201219507](https://doi.org/10.1051/0004-6361/201219507)
- McCracken, H. J., Wolk, M., Colombi, S., et al. 2015, *MNRAS*, 449, 901, doi: [10.1093/mnras/stv305](https://doi.org/10.1093/mnras/stv305)
- McLeod, D. J., McLure, R. J., Dunlop, J. S., et al. 2021, *MNRAS*, 503, 4413, doi: [10.1093/mnras/stab731](https://doi.org/10.1093/mnras/stab731)
- Moster, B. P., Naab, T., & White, S. D. M. 2018, *MNRAS*, 477, 1822, doi: [10.1093/mnras/sty655](https://doi.org/10.1093/mnras/sty655)
- Moster, B. P., Somerville, R. S., Maulbetsch, C., et al. 2010, *ApJ*, 710, 903, doi: [10.1088/0004-637X/710/2/903](https://doi.org/10.1088/0004-637X/710/2/903)
- Moster, B. P., Somerville, R. S., Newman, J. A., & Rix, H.-W. 2011, *ApJ*, 731, 113, doi: [10.1088/0004-637X/731/2/113](https://doi.org/10.1088/0004-637X/731/2/113)
- Moustakas, J., Coil, A. L., Aird, J., et al. 2013, *ApJ*, 767, 50, doi: [10.1088/0004-637X/767/1/50](https://doi.org/10.1088/0004-637X/767/1/50)
- Mowla, L., Iyer, K. G., Desprez, G., et al. 2022, *ApJL*, 937, L35, doi: [10.3847/2041-8213/ac90ca](https://doi.org/10.3847/2041-8213/ac90ca)
- Murray, S. G., Diemer, B., Chen, Z., et al. 2021, *Astronomy and Computing*, 36, 100487, doi: [10.1016/j.ascom.2021.100487](https://doi.org/10.1016/j.ascom.2021.100487)
- Muzzin, A., Marchesini, D., Stefanon, M., et al. 2013, *ApJS*, 206, 8, doi: [10.1088/0067-0049/206/1/8](https://doi.org/10.1088/0067-0049/206/1/8)
- Pillepich, A., Springel, V., Nelson, D., et al. 2018, *MNRAS*, 473, 4077, doi: [10.1093/mnras/stx2656](https://doi.org/10.1093/mnras/stx2656)
- Planck Collaboration, Aghanim, N., Akrami, Y., et al. 2020, *A&A*, 641, A6, doi: [10.1051/0004-6361/201833910](https://doi.org/10.1051/0004-6361/201833910)
- Pozzetti, L., Bolzonella, M., Zucca, E., et al. 2010, *A&A*, 523, A13, doi: [10.1051/0004-6361/200913020](https://doi.org/10.1051/0004-6361/200913020)
- Quadri, R. F., & Williams, R. J. 2010, *ApJ*, 725, 794, doi: [10.1088/0004-637X/725/1/794](https://doi.org/10.1088/0004-637X/725/1/794)
- Roche, N., & Eales, S. A. 1999, *MNRAS*, 307, 703, doi: [10.1046/j.1365-8711.1999.02652.x](https://doi.org/10.1046/j.1365-8711.1999.02652.x)
- Sabater, J., Best, P. N., Tasse, C., et al. 2021, *A&A*, 648, A2, doi: [10.1051/0004-6361/202038828](https://doi.org/10.1051/0004-6361/202038828)
- Santini, P., Castellano, M., Fontana, A., et al. 2022, *ApJ*, 940, 135, doi: [10.3847/1538-4357/ac9a48](https://doi.org/10.3847/1538-4357/ac9a48)
- Scharré, L., Sorini, D., & Davé, R. 2024, *MNRAS*, 534, 361, doi: [10.1093/mnras/stae2098](https://doi.org/10.1093/mnras/stae2098)
- Schaye, J., Crain, R. A., Bower, R. G., et al. 2015, *MNRAS*, 446, 521, doi: [10.1093/mnras/stu2058](https://doi.org/10.1093/mnras/stu2058)
- Schmidt, M. 1968, *ApJ*, 151, 393, doi: [10.1086/149446](https://doi.org/10.1086/149446)
- Scoville, N., Aussel, H., Brusa, M., et al. 2007a, *ApJS*, 172, 1, doi: [10.1086/516585](https://doi.org/10.1086/516585)
- Scoville, N., Aussel, H., Benson, A., et al. 2007b, *ApJS*, 172, 150, doi: [10.1086/516751](https://doi.org/10.1086/516751)
- Shuntov, M., McCracken, H. J., Gavazzi, R., et al. 2022, *A&A*, 664, A61, doi: [10.1051/0004-6361/202243136](https://doi.org/10.1051/0004-6361/202243136)
- Silk, J., & Rees, M. J. 1998, *A&A*, 331, L1, doi: [10.48550/arXiv.astro-ph/9801013](https://doi.org/10.48550/arXiv.astro-ph/9801013)
- Sinha, M., & Garrison, L. 2019, in *Software Challenges to Exascale Computing*, ed. A. Majumdar & R. Arora (Singapore: Springer Singapore), 3–20. https://doi.org/10.1007/978-981-13-7729-7_1
- Sinha, M., & Garrison, L. H. 2020, *MNRAS*, 491, 3022, doi: [10.1093/mnras/stz3157](https://doi.org/10.1093/mnras/stz3157)
- Somerville, R. S., & Primack, J. R. 1999, *MNRAS*, 310, 1087, doi: [10.1046/j.1365-8711.1999.03032.x](https://doi.org/10.1046/j.1365-8711.1999.03032.x)
- Springel, V., Frenk, C. S., & White, S. D. M. 2006, *Nature*, 440, 1137, doi: [10.1038/nature04805](https://doi.org/10.1038/nature04805)
- Springel, V., White, S. D. M., Jenkins, A., et al. 2005, *Nature*, 435, 629, doi: [10.1038/nature03597](https://doi.org/10.1038/nature03597)
- Stevens, A. R. H., Croton, D. J., & Mutch, S. J. 2016, *MNRAS*, 461, 859, doi: [10.1093/mnras/stw1332](https://doi.org/10.1093/mnras/stw1332)
- Stevens, A. R. H., Sinha, M., Rohl, A., et al. 2023, *arXiv e-prints*, arXiv:2312.04137, doi: [10.48550/arXiv.2312.04137](https://doi.org/10.48550/arXiv.2312.04137)
- Stewart, K. R., Bullock, J. S., Barton, E. J., & Wechsler, R. H. 2009, *ApJ*, 702, 1005, doi: [10.1088/0004-637X/702/2/1005](https://doi.org/10.1088/0004-637X/702/2/1005)
- Tasse, C., Shimwell, T., Hardcastle, M. J., et al. 2021, *A&A*, 648, A1, doi: [10.1051/0004-6361/202038804](https://doi.org/10.1051/0004-6361/202038804)
- Tinker, J. L., Leauthaud, A., Bundy, K., et al. 2013, *ApJ*, 778, 93, doi: [10.1088/0004-637X/778/2/93](https://doi.org/10.1088/0004-637X/778/2/93)

- Tinker, J. L., Robertson, B. E., Kravtsov, A. V., et al. 2010, *ApJ*, 724, 878, doi: [10.1088/0004-637X/724/2/878](https://doi.org/10.1088/0004-637X/724/2/878)
- Vogelsberger, M., Genel, S., Springel, V., et al. 2014, *MNRAS*, 444, 1518, doi: [10.1093/mnras/stu1536](https://doi.org/10.1093/mnras/stu1536)
- Wake, D. A., Whitaker, K. E., Labbé, I., et al. 2011, *ApJ*, 728, 46, doi: [10.1088/0004-637X/728/1/46](https://doi.org/10.1088/0004-637X/728/1/46)
- Wall, J. V., & Jenkins, C. R. 2012, *Practical Statistics for Astronomers*
- Weaver, J. R., Kauffmann, O. B., Ilbert, O., et al. 2022, *ApJS*, 258, 11, doi: [10.3847/1538-4365/ac3078](https://doi.org/10.3847/1538-4365/ac3078)
- Weaver, J. R., Davidzon, I., Toft, S., et al. 2023, *A&A*, 677, A184, doi: [10.1051/0004-6361/202245581](https://doi.org/10.1051/0004-6361/202245581)
- Wechsler, R. H., & Tinker, J. L. 2018, *ARA&A*, 56, 435, doi: [10.1146/annurev-astro-081817-051756](https://doi.org/10.1146/annurev-astro-081817-051756)
- Weinberger, R., Springel, V., Hernquist, L., et al. 2017, *MNRAS*, 465, 3291, doi: [10.1093/mnras/stw2944](https://doi.org/10.1093/mnras/stw2944)
- Wetzell, A., Hayward, C. C., Sanderson, R. E., et al. 2023, *ApJS*, 265, 44, doi: [10.3847/1538-4365/acb99a](https://doi.org/10.3847/1538-4365/acb99a)
- Wetzell, A. R., Cohn, J. D., & White, M. 2009, *MNRAS*, 395, 1376, doi: [10.1111/j.1365-2966.2009.14424.x](https://doi.org/10.1111/j.1365-2966.2009.14424.x)
- White, S. D. M., & Rees, M. J. 1978, *MNRAS*, 183, 341, doi: [10.1093/mnras/183.3.341](https://doi.org/10.1093/mnras/183.3.341)
- Zaidi, K., Marchesini, D., Papovich, C., et al. 2024, *ApJ*, 969, 84, doi: [10.3847/1538-4357/ad45fa](https://doi.org/10.3847/1538-4357/ad45fa)
- Zehavi, I., Weinberg, D. H., Zheng, Z., et al. 2004, *ApJ*, 608, 16, doi: [10.1086/386535](https://doi.org/10.1086/386535)
- Zehavi, I., Zheng, Z., Weinberg, D. H., et al. 2005, *ApJ*, 630, 1, doi: [10.1086/431891](https://doi.org/10.1086/431891)
- . 2011, *ApJ*, 736, 59, doi: [10.1088/0004-637X/736/1/59](https://doi.org/10.1088/0004-637X/736/1/59)
- Zheng, Z., Coil, A. L., & Zehavi, I. 2007, *ApJ*, 667, 760, doi: [10.1086/521074](https://doi.org/10.1086/521074)
- Zheng, Z., Berlind, A. A., Weinberg, D. H., et al. 2005, *ApJ*, 633, 791, doi: [10.1086/466510](https://doi.org/10.1086/466510)
- Zu, Y., & Mandelbaum, R. 2015, *MNRAS*, 454, 1161, doi: [10.1093/mnras/stv2062](https://doi.org/10.1093/mnras/stv2062)
- . 2016, *MNRAS*, 457, 4360, doi: [10.1093/mnras/stw221](https://doi.org/10.1093/mnras/stw221)